

ACCESS: Confirmation of a Clear Atmosphere for WASP-96b and a Comparison of Light Curve Detrending Techniques

CHIMA D. MCGRUDER,^{1,*} MERCEDES LÓPEZ-MORALES,¹ JAMES KIRK,¹ NÉSTOR ESPINOZA,² BENJAMIN V. RACKHAM,^{3,†}
MUNAZZA K. ALAM,⁴ NATALIE ALLEN,⁵ NIKOLAY NIKOLOV,² IAN C. WEAVER,¹ KEVIN ORTIZ CEBALLOS,^{1,‡}
DAVID J. OSIP,⁶ DÁNIEL APAI,^{7,§} ANDRÉS JORDÁN,⁹ AND JONATHAN J. FORTNEY¹⁰

¹*Center for Astrophysics | Harvard & Smithsonian, 60 Garden St, Cambridge, MA 02138, USA*

²*Space Telescope Science Institute (STScI), 3700 San Martin Dr, Baltimore, MD 21218, USA*

³*Department of Earth, Atmospheric and Planetary Sciences, and Kavli Institute for Astrophysics and Space Research, Massachusetts Institute of Technology, Cambridge, MA 02139, USA*

⁴*Carnegie Earth & Planets Laboratory, 5241 Broad Branch Road NW, Washington, DC 20015*

⁵*William H. Miller III Department of Physics and Astronomy, Johns Hopkins University, 3400 N Charles St, Baltimore, MD 21218, USA*

⁶*Las Campanas Observatory, Carnegie Institution of Washington, Colina el Pino, Casilla 601 La Serena, Chile*

⁷*Steward Observatory, The University of Arizona, 933 N. Cherry Avenue, Tucson, AZ 85721, USA*

⁸*Lunar and Planetary Laboratory, The University of Arizona, 1629 E. University Boulevard, Tucson, AZ 85721*

⁹*Facultad de Ingeniera y Ciencias, Universidad Adolfo Ibáñez, Av. Diagonal las Torres 2640, Peñalolén, Santiago, Chile[§]*

¹⁰*Department of Astronomy & Astrophysics, University of California, Santa Cruz, CA 95064*

ABSTRACT

One of the strongest Na I features was observed in WASP-96b. To confirm this novel detection, we provide a new 475–825 nm transmission spectrum obtained with Magellan/IMACS, which indeed confirms the presence of a broad sodium absorption feature. We find the same result when reanalyzing the 400–825 nm VLT/FORS2 data. We also utilize synthetic data to test the effectiveness of two common detrending techniques: (1) a Gaussian processes (GP) routine, and (2) common-mode correction followed by polynomial correction (CMC+Poly). We find that both methods poorly reproduce the absolute transit depths but maintain their true spectral shape. This emphasizes the importance of fitting for offsets when combining spectra from different sources or epochs. Additionally, we find that for our datasets both methods give consistent results, but CMC+Poly is more accurate and precise. We combine the Magellan/IMACS and VLT/FORS2 spectra with literature 800–1644 nm HST/WFC3 spectra, yielding a global spectrum from 400–1644 nm. We used the **PLATON** and **Exoretrievals** retrieval codes to interpret this spectrum, and find that both yield relatively deeper pressures where the atmosphere is optically thick at log-pressures between $1.3^{+1.0}_{-1.1}$ and $0.29^{+1.86}_{-2.02}$ bars, respectively. **Exoretrievals** finds a solar to super-solar Na I and H₂O log-mixing ratios of $-5.4^{+2.0}_{-1.9}$ and $-4.5^{+2.0}_{-2.0}$, respectively, while **PLATON** finds an overall metallicity of $\log_{10}(Z/Z_{\odot}) = -0.49^{+1.0}_{-0.37}$ dex. Therefore, our findings are in agreement with literature and support the inference that the terminator of WASP-96b has few aerosols obscuring prominent features in the optical to near-infrared (near-IR) spectrum.

Keywords: planets and satellites: atmospheres — planets and satellites: — stars: activity — stars: starspots — techniques: spectroscopic

1. INTRODUCTION

In-depth studies of exoplanetary atmospheres (exo-atmospheres) is a key pathway to obtaining more detailed insights about the formation and evolution of planetary systems. Many of these planets are in extreme environments not found in the solar system and understanding how their atmospheres are sculpted by such unique environments gives us detailed insights on the complex chemistry and physics at play. Examples

Corresponding author: Chima D. McGruder
chima.mcgruder@cfa.harvard.edu

* NSF Graduate Research Fellow

† 51 Pegasi b Fellow

‡ NSF Graduate Research Fellow
Ford Foundation Pre-doctoral Fellow

§ Millennium Institute for Astrophysics, Chile
Data Observatory Foundation, Chile

include the cause of observed temperature inversions in hot Jupiters (e.g. [Baxter et al. 2020](#); [Gandhi & Madhusudhan 2019](#)), the cause and composition of high altitude aerosols (clouds and/or hazes) (e.g. [Moses et al. 2011](#); [Wakeford et al. 2019b](#); [Gao et al. 2020](#)), and observed super sonic wind speeds (e.g. [Fromang et al. 2016](#)). Observing exo-atmospheres also can improve our understanding of the formation and evolutionary processes that exoplanets undergo, e.g., host disk dissipation rate (e.g., [Powell 2021](#)) and hot Jupiter migration timescales (e.g., [Moses et al. 2013](#); [Powell 2021](#)).

To improve our understanding of exoplanets, observations have had to push the performance of instruments, which were not designed with exo-atmosphere studies in mind, to their limits. This has also been the case for data analysis techniques aimed at removing both instrumental and astrophysical systematics both from space-based observatories (e.g. [Pont et al. 2013](#); [Sing et al. 2019](#)) and ground-based ones (e.g. [Gibson et al. 2012](#); [Yan et al. 2020](#)).

As expected in any developing field, there have been a number of cases with disagreeing results (e.g., [Southworth et al. 2017](#) and [Diamond-Lowe et al. 2018](#); [Sedaghati et al. 2017](#) and [Espinoza et al. 2019b](#); and [Sing et al. 2015](#) and [Gibson et al. 2017](#), [Gibson et al. 2019](#), and [McGruder et al. 2020](#)). These discrepancies are attributed to imperfect understanding of systematics, whether it be instrumental, observational, or astrophysical in nature. This highlights the importance of confirming features of interest via independent analyses in order to isolate spurious signals and instill more confidence in agreeing detections. This is particularly important in attempts to find correlations between atmospheric features and other system parameters, such as the cause of high-altitude aerosol formation in gas giants. There have been several studies attempting to find such a correlation (i.e. [Sing et al. 2016](#); [Heng 2016](#); [Stevenson 2016](#); [Fu et al. 2017](#); [Tsiaras et al. 2018](#); [Dymont et al. 2021](#)), with no clear answer yet (e.g. [Alam et al. 2020](#)).

WASP-96b ($M=0.48 M_J$, $R = 1.2 R_J$, $P = 3.425$ days, G8 host star, [Hellier et al. 2014](#)), is one of few exoplanets observed to-date to have little evidence supporting the presence of high-altitude aerosols in both optical ([Nikolov et al. 2018](#)) and near-infrared (IR, [Yip et al. 2021](#)) transmission spectra. An exoplanet with a transmission spectrum that can be modeled excluding high-altitude aerosols is also called a “clear” atmosphere, which does not mean the planet has no aerosols but little to no aerosols obscure the summed terminator’s spectrum. Other planetary atmosphere that can be explained without including high-altitude aerosols are

WASP-17b ([Sing et al. 2016](#)), WASP-39b ([Fischer et al. 2016](#); [Nikolov et al. 2016](#); [Wakeford et al. 2018](#); [Kirk et al. 2019](#)), WASP-62b ([Alam et al. 2021](#)), and WASP-94Ab ([Ahner et al. 2022](#)). Finding planets like these is essential for understanding the evolutionary, chemical, and physical processes underway in this class of planets because aerosols mute the features needed to probe exo-atmospheres. This is particularly challenging given that it is estimated only $\sim 7\%$ of hot Jupiters have clear atmospheres ([Wakeford et al. 2019b](#)). As such, it is vital to find and thoroughly study clear planets like WASP-96b. The optical transmission spectrum of WASP-96b was first observed by [Nikolov et al. \(2018\)](#) with VLT/FORS2 and recently [Yip et al. \(2021\)](#) combined the VLT/FORS2 spectrum with a near-IR spectrum derived using HST/WFC3 observations from GO program 15469 (PI: Nikolay Nikolov) to obtain a better picture of the planet’s clear nature. These studies report strong Na I and H₂O features with abundances of $-3.88^{+1.05}_{-0.82}$ and $-3.65^{+0.90}_{-0.94}$, respectively.

In this paper, we present a new optical transmission spectrum of WASP-96b derived from new observations obtained as part of ACCESS¹.

These observations are described in Section 2. We then combined the ACCESS observations with an independent re-analysis of the original VLT/FORS observations and the available near-IR observations to derive a new 400–1644 nm optical to near-infrared transmission spectrum for this planet and re-inspect its atmospheric properties via retrieval models.

To understand individual and relative performances of commonly used detrending methods, we also conduct a detailed comparison of two often-used techniques in ground-based transmission spectroscopy: (1) a Gaussian processes routine ([Gibson et al. 2012](#); [Weaver et al. 2020](#); [Yan et al. 2020](#); [McGruder et al. 2020](#); [Weaver et al. 2021](#)), and (2) common-mode correction followed by polynomial correction ([Gibson et al. 2013](#); [Nikolov et al. 2016](#); [Gibson et al. 2017](#); [Nikolov et al. 2018](#); [Carter et al. 2020](#)). We discuss these detrending techniques and their performance comparison in Section 3.

The remainder of this paper is structured as follows. Section 4 describes our methods for constructing the transmission spectra, and Section 5 outlines how we consider stellar activity affecting the transmission spectra. The spectra are then interpreted using retrievals in Sec-

¹ The Atmospheric Characterization Collaboration for Exoplanet Spectroscopic Studies (ACCESS) survey on the Magellan Telescopes ([Jordán et al. 2013](#); [Rackham et al. 2017](#); [Bixel et al. 2019](#); [Espinoza et al. 2019b](#); [Weaver et al. 2020](#); [McGruder et al. 2020](#); [Weaver et al. 2021](#); [Kirk et al. 2021](#))

tion 6. In Section 7, we present and discuss the retrieval analysis results, and contextualize WASP-96b within the exoplanet population in Section 8. We conclude in Section 9.

2. OBSERVATIONS

2.1. VLT/FORS2 Transits

We used two transit observations of WASP-96b on the nights of UT170729 and UT170822 (UTYYMMDD) with the Focal Reducer and Spectrograph (FORS2)² mounted on the 8.2m Very Large Telescope (VLT) in the European Southern Observatory on Cerro Paranal, Chile. These observations were originally collected, reduced, and published by Nikolov et al. (2018). For our re-analysis of this data, described in Section 3, we used the same extracted spectra produced in Nikolov et al. (2018), where additional detail of the data collection and extraction process can be found. Both observations were taken with the multi-object spectroscopy (MOS) mode and the same two-slit mask. Each slit in the mask was 22'' by 120'' and centered on the target and comparison star. Given the wide slits, the spectral resolution of the observations were determined by the seeing, with an average resolving power of $R \sim 600$. The first transit was observed using the bluer dispersive element, GRIS600B (600B), which had approximate spectral coverage of 360–620 nm. Contrary to Nikolov et al. (2018), we excluded the spectrum from 360–400 nm to avoid systematics caused by the low counts, where that region had over 85% fewer counts than the rest of the spectrum. The second night used the redder GRIS600RI (600RI) grism and the GG435 filter, producing an approximate spectral coverage of 520–835 nm.

2.2. Magellan/IMACS Transits

We observed two transits of WASP-96b as part of the ACCESS Survey³ on the nights of UT170804 and UT171108 with the Inamori-Magellan Areal Camera & Spectrograph (IMACS; Dressler et al. 2011) on the 6.5-m Baade Magellan Telescope at Las Campanas Observatory in Chile. Both transits were observed using the $8K \times 8K$ CCD mosaic camera at the f/2 focus, which provides a 27.4' field of view (FoV). We used a 300 line/mm grating at blaze angle of 17.5° , yielding a spectral coverage of 0.44–0.97 μm (without a filter). To reduce readout time and improve the duty cycle of the observations, we used 2×2 binning. Both observa-

tions used the FAST readout mode, which had a 29 s readout time and a 3 s overhead. The first observation had no filter, but we applied the GG495 filter (coverage 0.49–0.97 μm) for the second night to prevent second-order light contamination. The effect of second-order contamination on the first observation is discussed in Appendix A.

For each observation we used the MOS mode and designed a custom science mask with 10'' by 90'' slits for the target and a number of comparison stars in the field. Identical masks, but with slit widths of 0.5'' instead of 10'', were also designed for wavelength calibrations. The average seeing-limited resolving power of the observations were $R \sim 900$.

The comparison stars were selected using the same prescription described in Rackham et al. (2017). We consider a nearby star as a suitable comparison if it has a color difference with WASP-96 of $D < 1$, where

$$D = \sqrt{[(B - V)_c - (B - V)_t]^2 + [(J - K)_c - (J - K)_t]^2}$$

The uppercase letters in the equation correspond to the Johnson-Cousin apparent magnitudes of the stars, and the subscripts t and c indicate the target and comparison, respectively. The comparisons used in both the ACCESS and VLT/FORS2 observations are summarized in Table 1.

We limited observations of each transit to airmass below 2 during the full transit window to minimize differential atmospheric refraction effects, so we ended up with two full transits with additional out-of-transit baselines of 1.29 and 1.35 hours for the UT170804 and UT171108 transits, respectively. To maintain count levels of 25,000–35,000 ADU⁴, given the average seeing conditions at each night, we held exposure times constant to 60 seconds for transit UT170804 (average seeing of 1.55'') and 45 seconds for transit UT171108 (average seeing of 0.71''). A summary of each transit's observing conditions are given in Table 2.

Finally, we collected bias frames, quartz lamp flats, HeNeAr calibrations (using the 0.5'' by 90'' masks), each with the same binning as the science observations.

2.2.1. ACCESS Reduction Pipeline

We reduced the data using the ACCESS custom pipeline introduced in Jordán et al. (2013) and described in detail in Espinoza (2017). We first subtracted the bias level from each frame using the median of the overscan region. The pipeline also has the option of flat-fielding

² FORS instrument website

³ ACCESS generally acquires ≥ 3 transits of a target to reduce systematics and increase precision, but determined two sufficient when considering the already observed VLT/FORS2 transits.

⁴ This is well within the linearity limits of the IMACS CCDs (Bixel et al. 2019).

Table 1. Target and comparison star magnitudes and coordinates from the UCAC4 catalog (Zacharias et al. 2013). We used comparisons 14 and 15 for the analysis of both IMACS transits and comparison 1 for both FORS2 transits. Comparison 3 was in the IMACS slit but was over saturated and not used.

Star	RA	Dec	B	V	J	K	D
WASP-96	00:04:11.12	-47:21:38.25	13.25	12.51	11.27	10.91	0
COMP1	00:04:18.87	-47:16:31.05	13.52	12.88	11.76	11.41	0.1
COMP3	00:04:02.03	-47:14:49.87	12.19	11.28	9.1	9.67	0.94
COMP14	00:05:12.82	-47:03:37.02	13.87	12.98	11.40	10.85	0.24
COMP15	00:04:25.01	-47:00:42.96	13.86	13.17	11.93	11.44	0.14

Table 2. Observing log for WASP-96b data from *Magellan/IMACS*.

Night	Obs. Start/	Airmass	Frames	min/max
Start (UTC)	End (UTC)			seeing ["]
2017 Aug. 04	02:55/06:38	1.93–1.09	148	1.4/1.71
2017 Nov. 08	00:01/03:49	1.11–1.18	180	0.68/0.8

each frame using a master flat, but as with previous ACCESS datasets (e.g. Rackham et al. 2017; Bixel et al. 2019; McGruder et al. 2020; Weaver et al. 2021; Kirk et al. 2021), we found that flat-fielding worsens the photometric precision of the transit light curves, so we opted to not flat-field the data. The ineffectiveness of flat-fielding is likely due to the lack of sufficient flats needed for the high precision analysis. We collected 10 to 25 flats per night with 1 to 5 second exposures.

We then performed a bad-pixel correction using a bad-pixel map obtained from the flats. Any pixel with 10 times higher or lower photon noise relative to neighboring pixels was added to the map. The correction was done to the science images by replacing the value of each flagged pixel with a value interpolated from the neighboring pixels in the dispersion direction of the detector.

We traced each spectrum in the images by first using a second-order polynomial to identify each resolution element’s centroid (relative to both spatial and dispersion directions). Then a fourth-order polynomial was fit on the centroids in order to ensure the smoothness of the trace.

The sky background was subtracted using the median of the spectral counts outside of the central apertures for a given wavelength element. The appropriate aperture sizes were empirically determined to be 3.6'' (9 pixels) in radius for UT170804 and 3.2'' (8 pixels) for UT171108. The extracted spectrum was produced by summing the spectral profile within the central aperture in the spatial direction and subtracting the sky background.

A Lorentzian profile was used to fit each spectral line in the HeNeAr calibration spectra. The wavelengths of each line as a function of pixel position was then fit using sixth-order polynomials. The pipeline iteratively excluded deviant datapoints until the root mean square error value of the fit was less than 2 km s^{-1} ($\sim 0.05 \text{ \AA}$). This wavelength map was applied to each extracted spectrum.

We identified and removed cosmic rays by first creating a global median spectrum using the median of all the normalized spectra for each exposure. This normalized, median spectrum was used to compare against each individual normalized spectrum, and any counts in a spectrum more than 10σ greater than the global median spectrum (on a corresponding wavelength) were replaced by interpolating the counts at the appropriate wavelength from the preceding and following spectra in the time series.

It should also be noted that the pipeline is capable of doing optimal extraction (Marsh 1989). This could potentially be used in place of bad-pixel and cosmic-ray removal, as it effectively highlights and removes deviant counts (Allen et. al., in prep.). However, we tested this for both WASP-96 observations, and found very little difference between resulting spectra.

Figure 1 shows the median extracted spectrum for both nights. The final wavelength range used was 475–825 nm for UT170804 and 525–825 nm for UT171108 (see Fig. 1). Given the diminishing throughput on the edge of the spectra, the bluest wavelengths had too few counts to be useful. We also excluded data from 759.4–767.2 nm, a region of strong tellurics. Though the sky subtraction and dividing by the comparison(s) should in principle negate the telluric features, that region still had a drastic decrease in counts (and likely residual telluric-induced systematics). This made it difficult to properly fit a light-curve at that wavelength range. Unfortunately, this coincides with the K I doublet (centered at 768.15 nm). We also excluded wavelengths longer than 825 nm due to the diminishing throughput

and increase in tellurics (see Fig. 1). We could have attempted to obtain useful information from that range, but given that the available HST/WFC3/IR/G102 data (Yip et al. 2021) is not afflicted by any of these effects, we instead omit that wavelength range from the ACCESS analysis.

When using the f/2 mode, each stellar spectrum is dispersed on two CCD chips, causing a gap in the spectra (see Figure 1). Fortunately, all utilized spectra of the target and COMP14 fell on one chip. For COMP15, the gap was approximately between 5580–5675Å; however, that region still had COMP14 for systematic corrections.

2.3. HST WFC3 Transits

The HST data were obtained directly from Yip et al. (2021) (GO program 15469, P.I. N. Nikolov). It consisted of two transits, one on UT181218 with the G102 grism (0.8–1.1 μm) and another on UT181228 G141 (1.1–1.7 μm) grism. The raw spatially scanned spectra were reduced with *Iraclis* (Tsiaras et al. 2016). The quadratic limb-darkening parameters were obtained using the models of Claret et al. (2013) and the inclination ($i=1.486$ radians), semimajor axis relative to stellar radius ($a/R_s=8.84$), and orbital period ($P=3.4252602$ days) were all held fixed to parameters determined from Hellier et al. (2014) and Nikolov et al. (2018).

2.4. Photometric Monitoring

We compiled and analyzed available time-series photometry of the host star WASP-96 from the Transiting Exoplanet Survey Satellite (TESS, Ricker et al. 2014) and the All-Sky Automated Survey for Supernovae (ASAS-SN, Kochanek et al. 2017) to constrain the presence of star spots that could contaminate the transmission spectrum of WASP-96b.

TESS observed WASP-96 in 2-minute-cadence mode over 27 days during Sector 2 (between 23 August and 20 September 2018) and over 24 days in Sector 29 (between 26 August and 20 September 2020). To model its photometric modulation, we used the Presearch Data Conditioning Simple Aperture Photometry (Jenkins et al. 2016, PDCSAP) light curve obtained from the Barbara A. Mikulski Archive for Space Telescopes (MAST) portal. We masked the transit data using a period of 3.42526 days, initial mid-transit time (t_0) of 2458354.319946 BJD, and a transit window of 3.04 hours (25% buffer in duration)⁵. The resulting out-of-transit light curves have a median abso-

lute deviation (MAD) of 2.76 parts-per-thousand (ppt) and a peak-to-peak difference of 25.5 ppt for Sector 2 (17676 data points), and a MAD of 2.9 ppt and peak-to-peak difference of 37.3 ppt for Sector 29 (14252 data points). For our analysis of the TESS data, we binned every 100 observations together.

ASAS-SN observed WASP-96 in two filters. *V* filter observations were collected between April 2014 and September 2018. *g* filter observations were collected between September 2017 and February 2020. To remove deviating observations, we sigma-clipped points that deviated by more than 3σ from the mean. This led to excluding 11 of 921 and 27 of 1626 observations for the *V* and *g* filters, respectively. Because of the lower cadence of the ASAS-SN observations (~ 3 per day) compared to the TESS observations, their larger variance, and since we do not expect significant stellar modulation in a day, we weighted averaged observations taken on the same night. We then removed observations with uncertainties larger than 3 times the mean uncertainty, which led to six binned observations removed in *V* band, and seven in *g* band. The final light curves included 351 & 520 datapoints with MADs of 10.4 & 9.5 ppt and peak-to-peak differences of 83.5 & 96.5 ppt, respectively.

3. LIGHT-CURVE ANALYSIS AND COMPARISON OF DETRENDING TECHNIQUES

All the wavelengths used in each extracted spectrum obtained in Section 2.2.1 were summed for every exposure to construct a photometric white-light curve. Furthermore, binned-light curves were constructed by partitioning the spectra into distinct spectro-photometric bins that were used to determine the change in transit depth over wavelength (i.e., the transmission spectrum). The binning scheme was designed by considering spectro-photometric precision, the overlap of spectral bands from different observations, high telluric absorption regions, and the desire to properly probe for atmospheric features, such as a scattering slope, sodium, and potassium lines. The bins used to construct the transmission spectrum are shaded grey in Figure 1 and their wavelength coverages are listed in the first column of Table 8. An overview of the white-light and binned light curve detrending technique implemented for our final light curves is provided in sections 3.1 & 3.2. However a more detailed description of our detrending routines are given in Appendix B. This section ends (3.3) with an explanation of how we determined the best detrending methods for our data.

3.1. White Light Curve Fitting

Our first step in detrending the VLT/FORS2 and Magellan/IMACS white-light curves was a sigma clip-

⁵ where the transit duration of 2.445 hours was calculated using the system parameters of Yip et al. (2021)

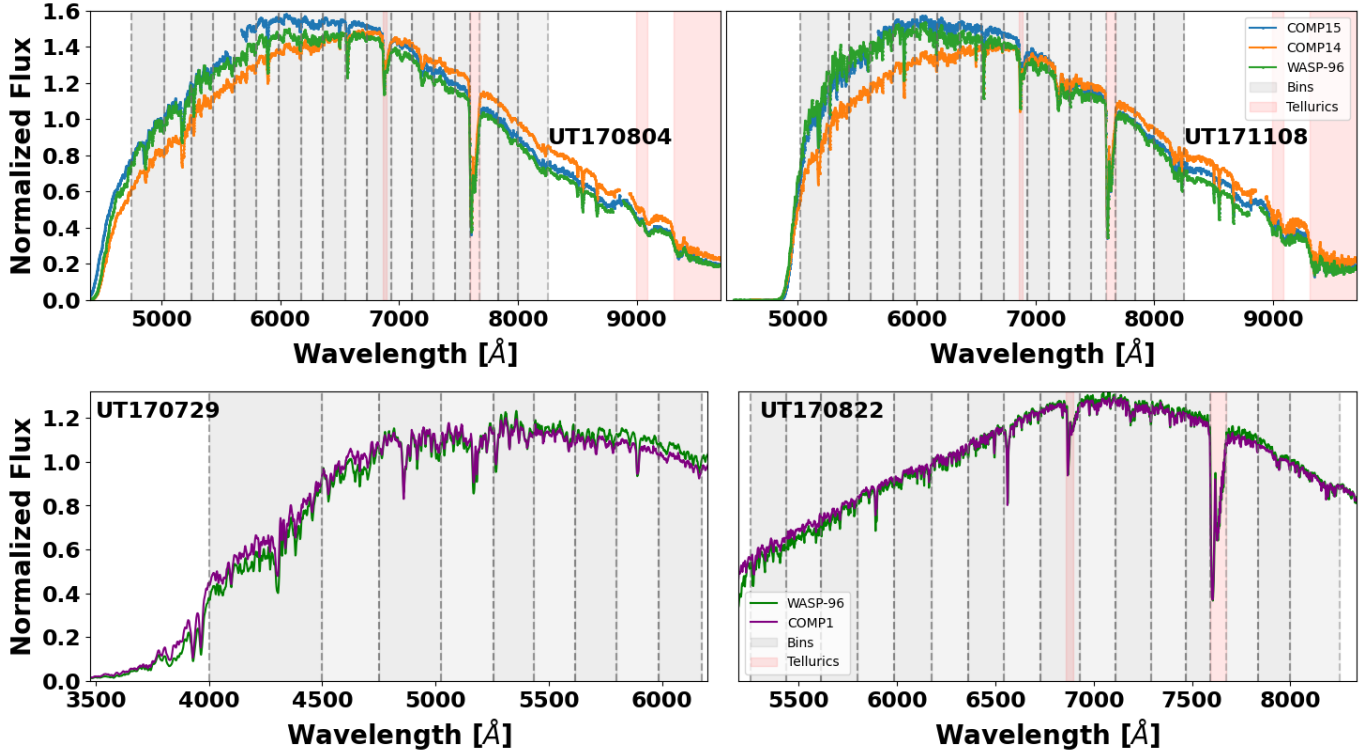


Figure 1. Median extracted spectra of WASP-96 and comparisons, excluding the oversaturated COMP 3. The top row shows IMACS data (UT170804 and UT171108) and the bottom shows FORS2 data from [Nikolov et al. 2018](#) (UT170729 and UT170822). Each spectroscopic bin used is shaded in light gray and demarked by dotted lines. Telluric regions with less than 0.1 transmission are shaded in light red. The only gap in the binning scheme is the strong telluric region from 7594.0–7672.0 Å.

ping of the raw light curves (target divided by mean of comparisons). This was done by individually evaluating each data point in the light curve with a moving average of 11 points centered around the point of interest. If the value of the specific point deviated by more than 3σ from the mean it was removed. We opted for this method because it does not depend on an initial transit model fit, which is often used as a sigma-clipping criteria. It resulted in zero, two, three, and two points being removed from each transit in chronological order.

We then used the PCA+GP routine (see Appendix B.1), to fit the sigma-clipped white-light curves. The transit parameters used in the fits were quadratic limb darkening (LD) coefficients, q_1, q_2 , planet orbital period, P , semi-major axis relative to the stellar radius, a/R_s , the planet-to-star radius ratio, R_p/R_s , impact parameter, b , mid-transit time, t_0 , eccentricity, e , and the argument of periastron, ω . q_1 and q_2 are parameterizations of the more commonly used u_1 and u_2 quadratic LD parameters, where $q_1 = (u_1 + u_2)^2$ and $q_2 = u_1/2(u_1 + u_2)$ ([Kipping 2013](#)). For our analysis we had to express b in terms of inclination, i , as

$$i = \cos^{-1} \left(\frac{b}{a} * \frac{(1 + e * \sin(\omega))}{1 - e^2} \right). \quad (1)$$

We adopted a circular orbit for WASP-96b, based on [Hellier et al. \(2014\)](#), and used a quadratic LD law as in [Nikolov et al. \(2018\)](#). We also held P (3.4252602 days), a/R_s (8.84), and i (1.486 radians) fixed to the values used by [Yip et al. \(2021\)](#) in order to later combine the optical and HST spectra. The quadratic LD parameters were set to be uniform from 0 to 1, and R_p/R_s had a normal prior with mean value of 0.115 and a standard deviation of 0.02. Here priors were based off of the R_p/R_s values obtained by [Nikolov et al. \(2018\)](#). For t_0 we used normal priors with uncertainties of 0.005 days (7.2 minutes) and mean values of $t_0 - 2,450,000 = 7963.33672$ [MJD], 7970.69261[BJD], 7987.31195[MJD], and 8066.59828[BJD] days for the transits in chronological order⁶. The best-fit white light curves and their corresponding orbital parameters are shown in Figure 2 and Table 3. We note that the difference in depth for the last transit (UT171108) is because the orbital parameters were held fixed. When allowed

⁶ small priors were used for the FORS2 data because they were based off of the t_0 values found by [Nikolov et al. \(2018\)](#). In order to use consistent priors for all transits, we fit the IMACS data first with wider priors (0.5 days, 12 hours), then with the 0.005 day priors after using the initial fit to obtain estimates on t_0 .

to be free, more consistent depths are obtained, and the other system parameter still agree within their uncertainty ranges. However, the absolute depth is not as relevant, as will be discussed in Section 3.3.

3.2. Binned light curve fitting

The next step on the path to produce the transmission spectrum is fitting the binned light curves to obtain values of R_p/R_s as a function of wavelength. With the uncorrected binned-light curves in hand, we first used the same 3σ clipping process discussed in Section 3.1 for each bin. Then the bins were detrended with a combination of common mode correction and polynomial fitting (CMC+Poly), where the CMC term (shown in Figure 2) was obtained from a PCA+GP fit of the white-light curve (detail in Appendix B.2). We also fixed all parameters, aside from q_1 , q_2 , and R_p/R_s , to values obtained by the PCA+GP white-light fit obtained in Section 3.1⁷. The bins used and their corresponding radii, along with plots of the raw (target/comparisons) and detrended light curves can all be found in Appendix D. We determined the CMC+Poly routine was best to detrend the binned light curves for this dataset, by testing its effectiveness against synthetic data, which is discussed in the following section (Sec. 3.3).

3.3. Comparing the performance of GP and CMC+Poly with Synthetic data

A number of techniques have been used to detrend the light curves of exoplanet transits (i.e. PCA e.g. Jordán et al. 2013, GP e.g. Gibson et al. 2012, CMC e.g. Gibson et al. 2013), but there are few instances in the literature that compare the effectiveness of one method over another (Gibson et al. 2013; Panwar et al. 2022, but they still do not compare against synthetic data). Furthermore, using two separate analysis techniques could produce widely different results (e.g. Sing et al. 2015 and Gibson et al. 2017). Thus, it is important to ensure the method utilized for a particular dataset yields as accurate results as possible and provides consistent uncertainty measurements. To instill confidence in our analysis procedures of the binned light curves, we synthesize transmission spectra to compare the precisions and accuracies of obtained transit depths to synthesized values. We test the synthetic data against two common transit reduction techniques: 1) a Gaussian Processes (GP) routine, and 2) Common-Mode-Correction followed by polynomial correction (CMC+Poly).

To test both methods, we created 500 synthetic light curves similar to the VLT/FORS2 observations. A detailed description of how the synthetic data were created can be found in Appendix E, but in general we simulated 50 flat (constant R_p/R_s) transmission spectra out of 10 bins each. All of the 10 bins had approximately the same shot noise levels (~ 400 ppm), which was assigned to produce a white-light curve noise level of about 125 ppm, consistent to the VLT/FORS2 white-light photon noise limits (~ 63 and 162 for transit UT170729 and UT170822, respectively). All bins in a given spectrum had the same overarching systematic generated by a random draw in a GP distribution, where the GP was constructed to be correlated to a few of the UT170729 observation’s auxiliary parameters. Then each individual bin had additional systematics generated from up to a second-order polynomial fit using other auxiliary parameters with random polynomial coefficients. Each bin also had their own quadratic limb darkening coefficients. Because the VLT/FORS2 observations only had one comparison star, we also only created one comparison star in our synthetic data. As outlined in Appendix B.1, when there is only one comparison star, PCA cannot be done and the PCA+GP routine becomes a GP routine with the comparison star used as a linear regressor. This is why in the synthetic analysis we refer to this method as a GP routine, but when using the same routine with the Magellan/IMACS data, which has two comparison stars, we refer to it as PCA+GP. Images of each step in the synthetic data production process are shown in Appendix E.

After the synthetic spectra were produced, we fit all 50 white light curves using the GP method in the same way described in Appendix B.1. We used the results of each white light curve as priors for the analysis of the binned light curves (see Appendix E). With those white-light parameters we produced the transmission spectra following first the GP process to detrend the bins, and then with the CMC+Poly process, which are both discussed in Appendix B. Both methods used to detrend the binned-light curves utilized the parameters determined from the GP detrended white-light data, and the CMC+Poly method used that white-light curve model to produce the CMC term. This allowed us to compare the effectiveness and accuracy of both methods given that each true depth is known. Additionally, because all 50 spectra were flat with the same inputted depth, we could collectively compare the results from every reduced bin.

To first understand the accuracies of both methods, we plot a histogram of the difference of each bin’s obtained depth relative to the true depth ($R_p/R_s = 0.1157$),

⁷ P , a/R_s , and i were already fixed to the values used by Yip et al. (2021)

Table 3. Fitted white light curve values. The period ($P=3.4252602$), semi-major axis (relative to stellar radius, $a/R_s=8.84$), and inclination ($i=85.14$) were all held fixed to parameters used by Yip et al. (2021). The mid-transit times are in terms of MJD for the FORS2 observations (UT170729 and UT170822) and BJD for the IMACS observations (UT170804 and UT171108). Note: the difference in depth for the last transit is because the orbital parameters were held fixed, when allowed to be free more consistent depths are obtained.

parameter	definition	UT170729	UT170804	UT170822	UT171108
R_p/R_s	planet radius/star radius	$0.1148^{+0.0029}_{-0.0033}$	$0.1168^{+0.0046}_{-0.0048}$	$0.1188^{+0.0015}_{-0.0018}$	$0.1018^{+0.0049}_{-0.0051}$
$t_0 - 2.45e6$	mid-transit (JD)	$7963.33662^{+0.00050}_{-0.00048}$	$7970.69093^{+0.00049}_{-0.00046}$	7987.31216 ± 0.00024	$8066.59703^{+0.00069}_{-0.00071}$
q_1	LD coeff 1	$0.37^{+0.10}_{-0.12}$	$0.23^{+0.11}_{-0.09}$	$0.31^{+0.06}_{-0.05}$	$0.32^{+0.18}_{-0.15}$
q_2	LD coeff 2	$0.29^{+0.24}_{-0.15}$	$0.33^{+0.34}_{-0.23}$	$0.63^{+0.18}_{-0.22}$	$0.31^{+0.32}_{-0.21}$

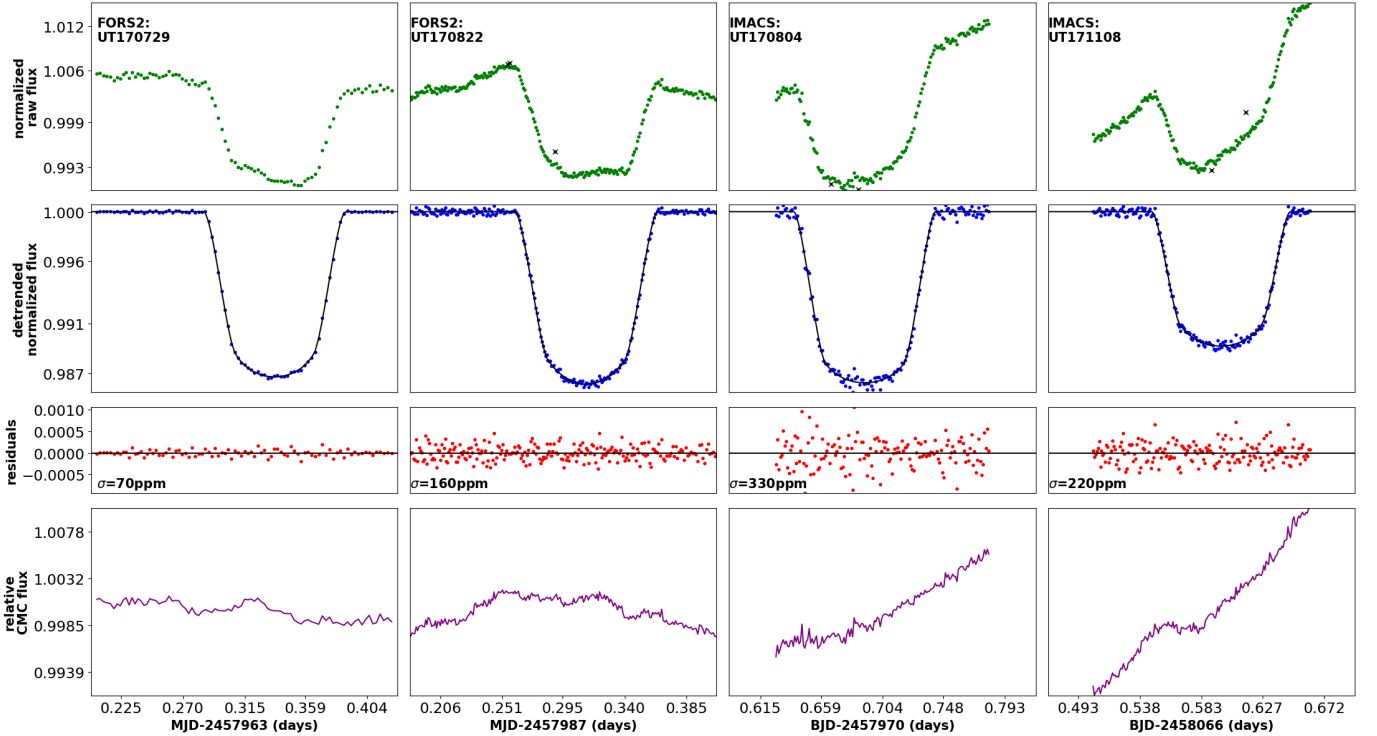


Figure 2. **Top:** White light curves (LC) composed from dividing the target by the sum of comparison stars, i.e., the raw LC. The first two columns are for the VLT/FORS2 transits, showing the exact data of Nikolov et al. (2018). The last two columns are new Magellan/IMACS observations directly from ACCESS’s custom pipeline. The data points marked with an x were identified as outliers and are not included in the rest of the analysis. **Middle:** The detrended white LC (blue points) produced utilizing our PCA+GP routine, the corresponding best-fit transit LC (solid black line) with orbital parameters shown in Table 3, and the residuals (red points) produce by subtracting the detrended data from the model. The value of σ given on each residual panel is the standard deviation of the residuals in ppm. **Bottom:** The common mode correction term, which was produced by dividing the top LC by the best fit transit model (the black LC in the middle panel, see Appendix B.2 for detailed discussions). This term was used to correct for common systematics in the binned light curves.

shown in the first column of Figure 3. From this we see that though the true depth is on average obtained using the GP method (first row), neither method consistently reproduced the true depths, where only $46.32 \pm 2.82\%^8$

⁸ uncertainties obtained through bootstrapping.

of the bins detrended using the GP method obtained a depth 1σ from its average uncertainties levels. The mean uncertainty of obtained R_p/R_s with the GP method was 0.00774. This is significantly worse using the CMC+Poly method, which only has $12.54 \pm 2.00\%$ of the bins within its 1σ level, where the mean uncertainty with the CMC+Poly method was 0.00127. This suggests that

if one were to fit any given transmission spectrum with the GP routine there is only a $46.32 \pm 2.82\%$ likelihood of those obtained depths being consistent with the physical depths. This is only worse using the CMC+Poly method. One likely strong contribution for this is that the bins are already biased by the white-light fit, given that the bins reduction is dependent on the white-light's. This is especially the case for the CMC method, because the common mode term, which drives the binned light curves correction model, can only be determined from the white-light fit. To support this we compared the obtained binned depths relative to their corresponding white-light fits' depths and find much more consistency of the depths with $41.79 \pm 2.82\%$ and $57.28 \pm 2.88\%$ within the 1σ average uncertainty for the CMC+Poly and GP methods, respectively.

Still, neither method can consistently re-obtain the true white-light depths. However, when comparing each bin to a corresponding mean depth determined by averaging all 10 bins for a given transmission spectrum (column two of Figure 3), we find $78.21 \pm 2.42\%$ and $70.72 \pm 2.67\%$ are within 1σ for the CMC+Poly and GP methods, respectively. This implies that though the absolute depth is not consistently obtained, a relative depth is for both detrending methods. If that is the case, it provides justification for the required offsets often needed when combining transmission spectra from different nights and/or different instruments (e.g. McGruder et al. 2020; Weaver et al. 2021; Yip et al. 2021). These results would also explain why the inconsistency in white-light depth found for transit UT171108 (Table 3 and Fig. 2) does not imply that the transmission spectrum of that night is incorrect. The likely scenario for that dataset is the GP routine misestimated the white-light depth (likely because of the fixed parameters), but this is common for the majority of the synthetic data as well. However, the relative binned depths can still be preserved using this white-light depth for the CMC correction, because the difference in depths from one bin to another is still maintained.

To further highlight that the structure of the spectrum is preserved we plot the standard deviation of all bins in a given spectrum. Since, each synthesized spectrum is flat, each bin (of a given spectrum) should not significantly vary from one another. This is exactly what we find, where every spectrum has a bin standard deviation significantly lower than that spectrum's average R_p/R_s uncertainty width (see column three of Figure 3). Furthermore, the third column shows that the standard deviation is higher for the GP method, implying that the CMC+Poly method is more consistent. Additionally, because the CMC+Poly method inherently pro-

duces lower uncertainties (average R_p/R_s uncertainty of 0.00127 for CMC+Poly compared to 0.00774 for GP), for this set of data, the CMC+Poly method is consistently more accurate and precise than the GP method. As such we elect to use the CMC+Poly method to detrend all binned light curves.

It is important to understand that these findings are only for this specific dataset, which is constructed to mimic the particular VLT/FORS2 observations of WASP-96b; i.e. the synthetic data has a relatively low shot noise level (~ 400 for bins), the bulk of the systematics are dominated by the white-light systematics (see Appendix E), and there was only one comparison star used. Therefore, this should not be extrapolated to every dataset. For example, we reduced the VLT/FORS2 data with just a CMC correction and found a similar fit compared to using CMC+Poly, outlining how little chromatic systematics persists in the given VLT/FORS2 data. If chromatic systematics are more dominant in a dataset or there are multiple comparison stars, then it could be possible that the data would be better reduced with a method like PCA+GP, which is less heavily dependent on the initial white-light fit. For this reason, we still ran the ACCESS data through both the CMC+Poly and PCA+GP routines as described below to confirm CMC+Poly still performed better for those data. In summary, one should explore the best detrending method for specific data before assigning one.

4. OPTICAL TRANSMISSION SPECTRUM FROM THE VLT/FORS2 AND ACCESS DATA

We produced the transmission spectrum by plotting the R_p/R_s found from each detrended binned-light curve against that wavelength interval (bin). Three optical transmission spectra were created. One from combining the two FORS2 transits where we weighted averaged all overlapping bins, another from combining the two IMACS transits, and the third from combining all four transits (global optical spectrum). These are plotted in Figure 4. As justified in Section 3.3, we fit an offset when combining each of the spectra. For a given combined spectrum a white-light depth was determined for each individual spectrum using a weighted mean of only overlapping bins. The weighted mean of these white-light depths was then used as the central depth for which each individual spectra was offset to. The average precision of each bin for the combined IMACS, FORS2, and global optical spectra are 0.00129, 0.00094, and 0.00076 R_p/R_s , respectively.

The IMACS data has more scatter and lower precision than the FORS2 data (see Fig. 4), even though both use two transits. One explanation to this is that the size

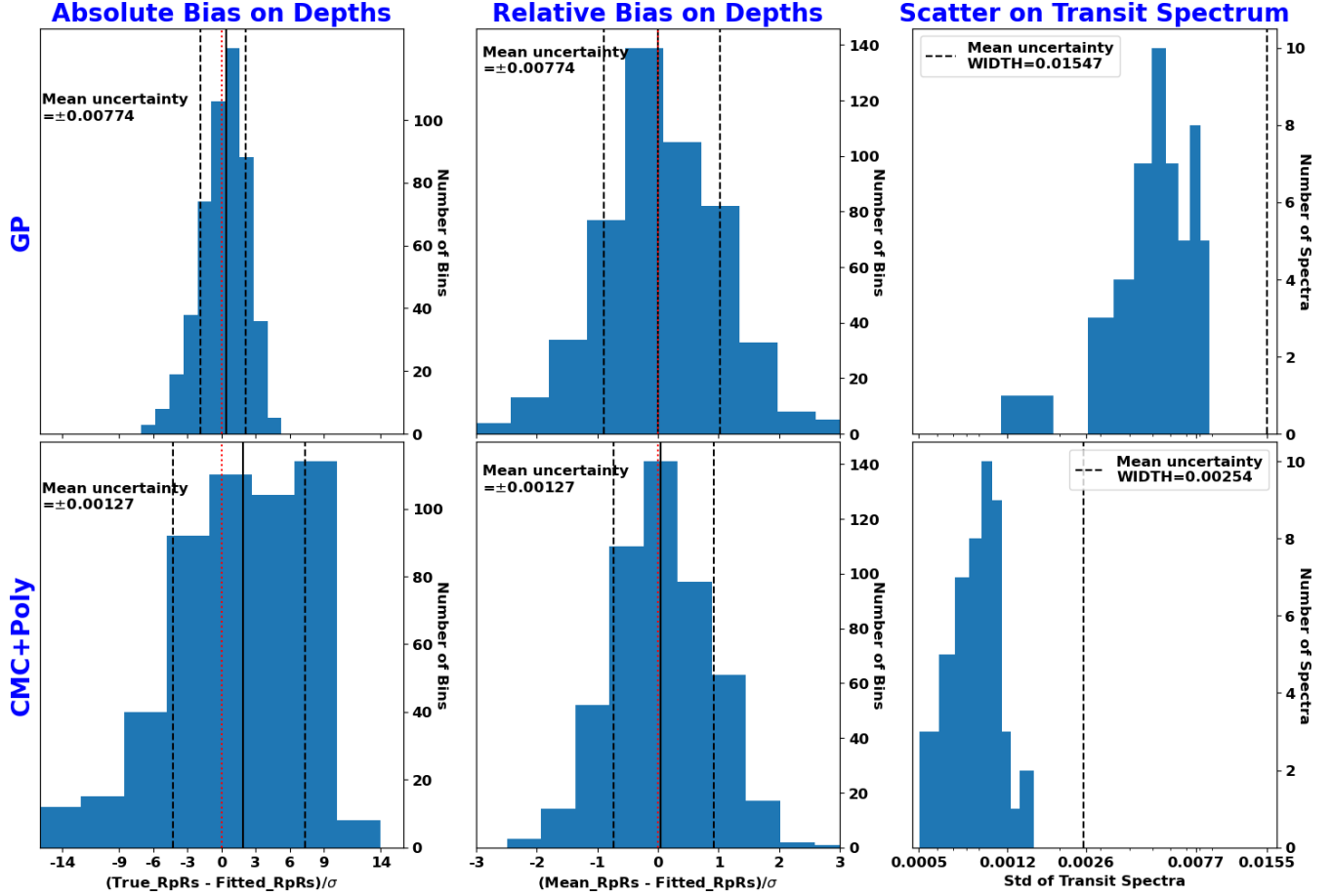


Figure 3. Histograms used to outline the biases and precisions of both the GP (top row) and the CMC+GP (bottom row) routines. **Left column:** We fit each of the 500 total synthetic binned light curves using the GP and CMC+Poly routines; then take the difference of each fitted binned depth from the true depth ($R_p/R_s=0.1157$) used to produce all synthetic data. That difference was divided by the uncertainty of the fitted depth, in order to obtain the bias from the input depth, relative to the uncertainties. The distribution of the relative differences are plotted. **Middle column:** This is similar to the left column, but instead is the difference of each fitted binned depth from the mean depth of all 10 bins in its corresponding transmission spectra. This provides a relative bias on obtained transit depths. In this case ‘relative’ means relative to the transmission spectrum’s mean depth. For both the left and middle columns, the black dashed line represents the average 16 and 84 percentiles of the histograms, the middle solid black line is the 50 percentile, and the red dotted line is 0. This corresponds to the true value of the depth, thus when the dashed black line and dotted red line do not overlap the routine has an inherent bias on that obtained depth. **Right column:** This is the standard deviation of each of the 50 transmission spectra. It shows the measured scatter of the transmission spectra, where the true scatter is 0, because the spectra were made to be flat. Here the black dashed line is the mean width of all bins uncertainties. Note that though both routines produce scatter well under their respective mean uncertainty widths, because the mean uncertainty width is over 6 times larger for the GP routine, the CMC+Poly routine is much more precise.

of Magellan Baade (6.5 m) is smaller than VLT (8.2 m), meaning less collecting area and more shot noise. Additionally, the difference in comparisons used could cause the IMACS data to have more systematics. The comparison [Nikolov et al. \(2018\)](#) used ($D=0.1$) was more similar to the target than either of ours ($D=0.24$ and 0.14 ; see [Table 1](#)). The importance of the comparisons is emphasized by [Ahrer et al. \(2022\)](#), where they were able to detect a strong sodium signal and a super-Rayleigh scattering slope in the atmosphere of WASP 94Ab with just

one comparison and one transit, partially attributed to the comparison being nearly identical in spectral type and location in the sky. Furthermore, for both IMACS transits the baselines, which is needed to properly correct for systematics, were relatively short (seen in [Fig 2](#)), where ideally the baseline should be the same length as the transit duration.

Likely the largest cause of deviation between the two datasets is that the IMACS data has more chromatic systematics. This can be seen when looking at the

binned light curves in Appendix D. Why the chromatic systematics are stronger for the IMACS observations is unclear. It might be due to chromatic differences in comparisons, or some other issue. Regardless, the CMC method relies on the assumption that the bulk of the systematics found in the white-light curve can be applied to each of the binned light curves. If each bin's systematics are more unique the initial CMC is not as effective, and might even introduce more spurious signals that the polynomial fit has to correct for. Concern over this led us to analyze the IMACS data with both CMC+Poly and PCA+GP routines. In doing so we found that the two transmission spectra were consistent to one another, with each bin deviating from one another by 0.562σ on average. However, the uncertainties of the PCA+GP method were nearly 5 times larger than the CMC+Poly's. Given both methods produced similar features, the accuracy of the CMC+Poly method is supported by Section 3.3, and the desire to use the same routine for all datasets we choose to continue using the CMC+Poly routine for the IMACS data.

5. STELLAR ACTIVITY

Activity in the host star can introduce signals into the planetary transmission spectrum (Pont et al. 2008; Berta et al. 2011; Oshagh et al. 2014; Rackham et al. 2017; Alam et al. 2018; Wakeford et al. 2019a; Rackham et al. 2022). Therefore, in order to prevent misinterpretation of WASP-96b's transmission spectrum, we parameterize the host star's level of activity. The three proxies for stellar activity we explore are 1) rotational period (Pallavicini et al. 1981), 2) Ca II lines (Vaughan & Preston 1980; Middelkoop 1981; Noyes et al. 1984), and 3) photometric modulation (e.g., Kipping 2012; Weaver et al. 2020).

5.1. Rotational Period

We infer the stellar rotational period by combining the radius of the star with the projected stellar rotational velocity, $v \sin i$, as well as fitting a periodic signal to the photometric monitoring data. The $v \sin i$ for WASP-96 was determined by Hellier et al. (2014) using the Euler/CORALIE spectrograph. It was not well constrained but was found to be $1.5 \pm 1.3 \text{ km s}^{-1}$. This provides a $3\text{-}\sigma$ upper limit on $v \sin i$ of 5.4 km s^{-1} . Combining this with the stellar radius of $1.05 \pm 0.05 R_{\odot}$ (Hellier et al. 2014) we estimate a $3\text{-}\sigma$ lower limit on rotation period of about 9.8 days. Thus, we scanned the photometric data for periodic peaks within a range of 9.8 to 300 days using Lomb-Scargle periodogram analysis (Lomb 1976). With the binned combined TESS data the highest periodic peaks were 35.9, 37.7, and 31.2, and with the combined

ASAS-SN data they were 28.3, 28.8, and 11.2. However, for all peaks the False Alarm Probability (FAP) were greater than 10^{-1} , thus no significant peaks were found with the periodogram analysis. This is likely because the photometric modulation is in general very small (see Sec. 2.4 or Sec. 5.3).

We then jointly fit the ASAS-SN and binned TESS data using the *Juliet* package (Espinoza et al. 2019a) with a semi-periodic kernel. In this joint fit, only the period and timescale terms (see equation 9 of Espinoza et al. (2019a)) are set common for all photometric campaigns. All other parameters were specific to the combined TESS (sector 2 and 29), the V band ASAS-SN, or the g band ASAS-SN data. When doing this we assume the periodicity is due to stellar inhomogeneities⁹ coming in and out of view as the star rotates, which is often done (e.g., Hirano et al. 2012; Sing et al. 2015; Newton et al. 2018). We use wide uniform priors on the period from 9.8 to 50 days, which is consistent with what the periodograms and $v \sin i$ weakly suggest. The resulting period was found to be $31.3^{+0.3}_{-3.4}$ days. Given the observed correlation of rotational period to activity levels (e.g. Pallavicini et al. 1981; Reiners et al. 2014), this also implies that WASP-96 is a relatively quiet star. Figure 5 shows the photometric monitoring campaigns along with the *Juliet* best fits.

5.2. Ca II H & K lines

The Ca II H & K lines were measured using two $R = 48000$ spectra collected with the MPG 2.2-m/FEROS spectrograph on 19 December 2016. Each spectrum has an average SNR of 27. The reduced data was acquired from ESO's online archive. Figure 6 shows the Ca II H & K lines and we see no emission in the core of either of the lines, implying that WASP-96 is a relatively inactive star.

5.3. Photometric Modulation

The analysis in the above two subsections suggest that WASP-96 is a quiet G-type star. However, we use the amplitude of the photometric modulation of the star to quantify its level of activity in terms of spot covering fraction and spot temperature, which are the parameters needed for the retrievals (see Sec. 6). This is done by using equation 2 and Table 2 of Rackham et al. (2019) and twice the TESS MAD of 0.0058 (see Sec. 2.4), assuming that the MAD is approximately the amplitude of sinusoidal variation. We use the TESS data because the vari-

⁹ Even with a relatively quiet star like WASP-96, we are assuming that smaller spots/faculae can be used to measure modulation and rotational period.

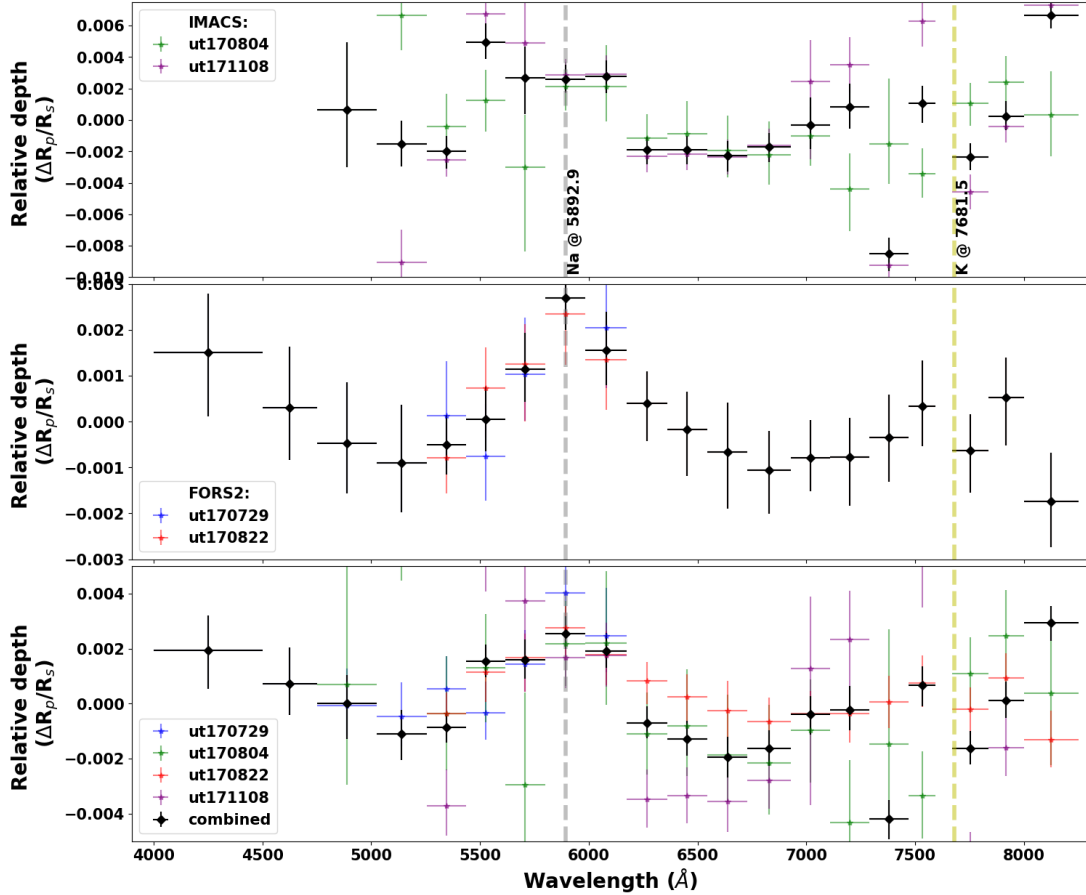


Figure 4. The transmission spectra using only the two Magellan/IMACS transits (top), only the two VLT/FORS2 transits (middle), and combining all four transits (bottom). In all three plots the black points correspond to the final spectrum produced by taking the weighted average of all overlapping bins. When combining each spectrum an offset is applied, so the means of each individual spectra are consistent, before the bins are averaged together. The center of the Na I and K I absorption are plotted as dotted gray and yellow lines, respectively.

ability in the ASAS-SN data seems to be driven by more than just the star (likely low precision), which is apparent when comparing the MAD of the TESS and ASAS-SN monitoring campaigns of the same target. Following that procedure, we estimate a spot covering fraction of WASP-96 $1.35 \pm 0.97\%$ assuming only spots are present and $1.40 \pm 1.09\%$ assuming spots and faculae are both present.

To capture these limitations in the retrieval analysis, we constrained the heterogeneity covering fraction, f , to have normal priors with a mean of 0.014 and standard deviation of 0.009. For a G8 star like WASP-96, we should expect the heterogeneity temperature contrast, ΔT , to be roughly 1600 K (see Berdyugina 2005; Rackham et al. 2019). We used wider uniform priors from -3000 to 3000 K on ΔT , see Appendix F.

6. RETRIEVAL ANALYSIS

We combined each of the three optical spectra discussed in Section 4 (IMACS only, FORS2 only, and

global spectra, see Fig. 4) with the HST/WFC3 data. We ran each of these three optical to near-IR spectra against two retrievals: **PLATON** (v3, Zhang et al. 2019) and **Exoretrievals** (introduced in Espinoza et al. 2019b). We used both **PLATON** and **Exoretrievals**, because their differing approaches of modeling exo-atmospheres provides different insights about the observed transmission spectra. The key differences between **PLATON** and **Exoretrievals** are: (1) **PLATON** includes collision induced absorption, where **Exoretrievals** does not, (2) **Exoretrievals** models the transmission spectrum using a semi-analytical formalism with an isothermal, isobaric, atmosphere and non-equilibrium chemistry, but **PLATON** uses an isothermal atmosphere and imposes equilibrium chemistry¹⁰,

¹⁰ Though equilibrium chemistry, might be an inaccurate assumption for observed transmission spectral features (e.g. Venot et al. 2012; Komacek et al. 2019; Roudier et al. 2021), using it still

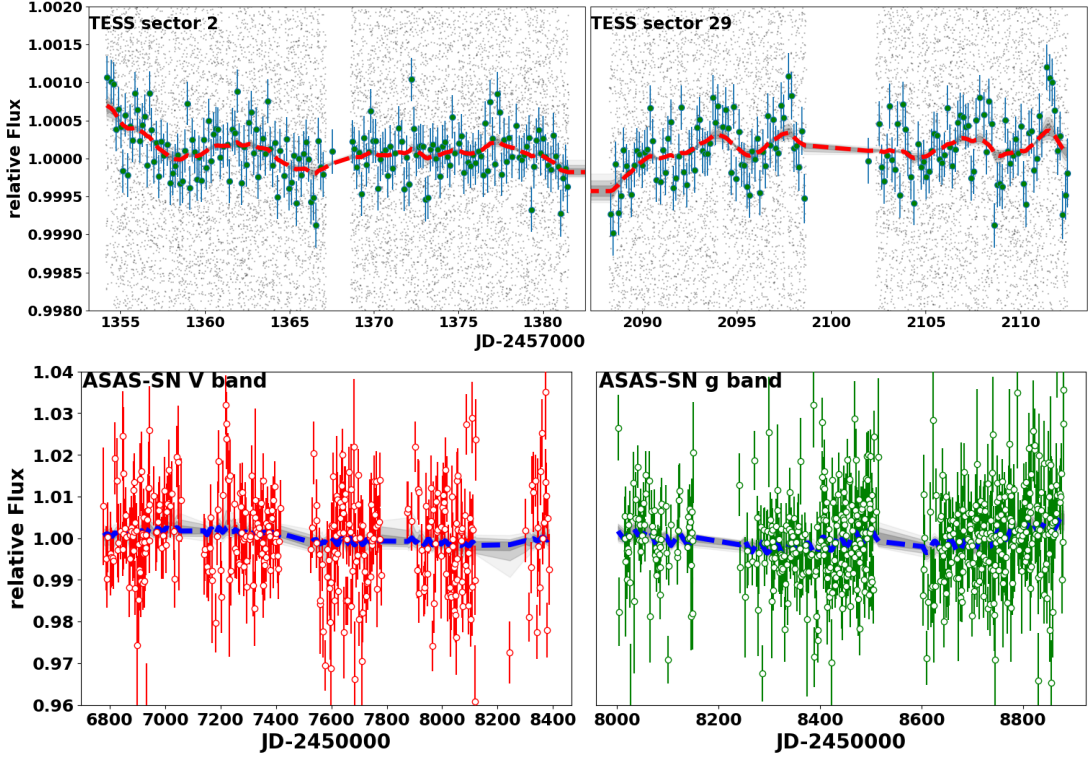


Figure 5. Photometric monitoring of WASP-96: The top row is TESS monitoring. There the red dashed lines are the *Juliet* semi-periodic best fit. The grey dots are the original 30-minute cadence TESS observations and the green dots are the data at 100 (~ 3.34 hours) binning, with their associated error bars in blue. The right figure is sector 29 data and the left is from sector 2, where both sectors were combined to act as one dataset for the *Juliet* fit (the binned data was used for the fitting). The bottom row is ASAS-SN monitoring, where the blue dashed lines are the *Juliet* semi-periodic best fit. On the right, the green hollow circles with associated error bars correspond to the g band data. On the left, the red hollow circles with associated error bars correspond to the V band data. The V and g band data were used as separated datasets in the *Juliet* fit. For all *Juliet* fits (blue and red dotted lines), there is a gradient of shaded gray regions representing the 1,2,& 3 sigma confidence intervals. For the TESS data, the confidence intervals are about the size of the dotted line.

and (3) the bulk of the line list used by PLATON are from HITRAN (Rothman et al. 2013), whereas the majority of what Exoretrievals uses is from HITEMP (Rothman et al. 2010) and ExoMol (Yurchenko et al. 2013; Tennyson et al. 2016). Additionally, testing a transmission spectrum against multiple retrievals provides a robustness against assumptions that are unique to each retrieval (e.g. McGruder et al. 2020; Kirk et al. 2021).

Both retrievals used nested sampling to explore their parameter space (dynesty, Speagle 2020, for PLATON and PyMultiNest, Buchner et al. 2014, for Exoretrievals), as such we used the differences in log Bayesian evidences, $\Delta \ln Z$, to test which specific model was favored over another. Following the same prescription as McGruder et al. 2020 (from Trotta 2008; Benneke & Seager 2013), we interpreted the $\Delta \ln Z$ values in a frequentist significance as: $|\Delta \ln Z|$ of 0 to 2.5 is

inconclusive with $< 2.7\sigma$ support for the higher evidence model, $|\Delta \ln Z|$ of 2.5 to 5 corresponds to a moderately significant detection of 2.7σ to 3.6σ , and $|\Delta \ln Z| \geq 5$ corresponds to strong support for one model over the other.

With Exoretrievals, we tested the spectra against having either water, potassium, sodium, water and sodium, and all three species in the transmission spectra. Along with these molecular and atomic species, we tested if the spectra warranted high altitude scattering agents, stellar activity, and a combination of scatters and activity. Lastly, a model with no features (flat spectrum) and only activity features was tested. In total, we tested 22 different combinations of models. For all models, aside from the flat spectrum, a reference radius (parameterized with f) and reference pressure (P_0) were fit. These are the pressure and corresponding radius where the atmosphere is optically thick in all wavelengths.

With PLATON we tested a model with scattering agents, stellar activity, models with both scattering

provides useful insights that could not be obtained without this assumption.

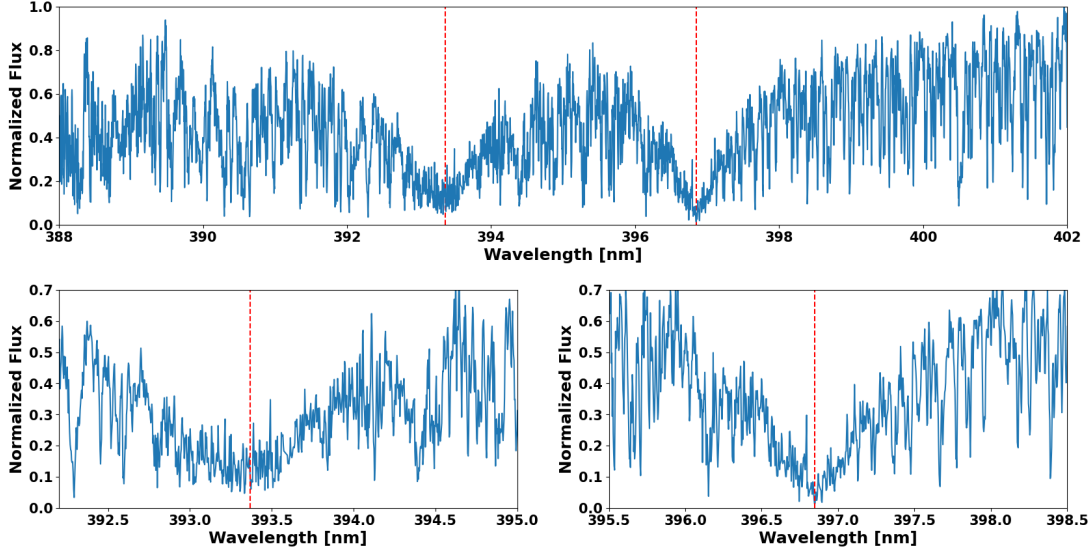


Figure 6. High-resolution FEROS spectrum of WASP-96: Both Ca II H & K lines (top), where the dashed red lines correspond to the K line core centered at 393.366 nm and the H line core centered at 396.847 nm. The left bottom panel is zoomed in on the K line and the bottom right is zoomed in on the H line, with the central cores highlighted with red dotted lines in both. There is no emission seen in either of the cores.

agents and stellar activity, and a model without either (clear). All models fit for a reference radius (R_0) corresponding to the radius of the planet at an arbitrary reference pressure, which was set to 1 bar. The models also fit for a pressure (P_{cloud}) where the atmosphere is optically thick.

The priors did not change for each spectrum we ran against the retrievals and we set the priors between **PLATON** and **Exoretrievals** as consistent to one another as possible. For all three spectra and both retrieval models we fit an offset between the optical and near-IR data¹¹, which is justified given that the detrending method used for the optical data does not preserve absolute depth (see Sec. 3.3).

6.1. IMACS & FORS2 Transmission Spectra

Tables of $\Delta \ln Z$ for both datasets against both retrievals are shown in Tables 4 & 5. In the tables the $\Delta \ln Z$ values for each model was determined by comparing the clear model, for **PLATON**, or the clear model and flat spectrum, for **Exoretrievals**, to the other models. One can also compare any given model from another by examining the difference of $\Delta \ln Z$'s between one another.

Using **Exoretrievals**, we find from both the IMACS and FORS2 spectra, independently, that the model with the highest $\Delta \ln Z$ is one with water and sodium (no potassium). We find that models with additional stellar

activity or scatters do not make a significant difference in the $\Delta \ln Z$, aside for the IMACS dataset that has a significant decrease in $\Delta \ln Z$ when including scatters ($\Delta \ln Z$ decreases by 4, compared to a model with only water and sodium). The feature blue-ward of 500 nm is likely what the retrievals with scatters and activity are attempting to fit. However, because the feature is not extreme, relative to the uncertainties (especially for the IMACS dataset), there is not sufficient support for the extra complexity of these models. As such we can only claim a tentative detection of a slight blue-ward slope either attributed from the star or a possible Rayleigh scattering slope. For the IMACS data the best fit model that included stellar activity found spot parameters of $\Delta T = -150^{+1300}_{-1700}$ K and $f = 0.0114^{+0.0085}_{-0.0072}$. For FORS2 those activity parameters were $\Delta T = -1060^{+1100}_{-1200}$ K and $f = 0.0124^{+0.0083}_{-0.0080}$. The best model which included a haze scattering slope for the IMACS data obtained a haze power law of $\gamma = -9.3^{+7.8}_{-3.4}$, and $\gamma = -9.7^{+5.1}_{-3.0}$ was obtained for the FORS2 best scatters model. With **Exoretrievals** γ of -4 corresponds to a Rayleigh slope (see Appendix D of Espinoza et al. (2019b)), implying that even though the retrieved slopes are unconstrained, they are consistent with Rayleigh scattering. The detections of H_2O and Na were highly significant ($\Delta \ln Z > 11$) for both datasets. The highest-evidence retrieval model parameters for this data subset and the others can be seen in Table 6

Interestingly, with **PLATON** there is less consistency amongst the two datasets. All **PLATON** models with the FORS2 dataset were indistinguishable from one another,

¹¹ **PLATON** v3 could not fit an offset between different dataset, as such, we modified the code to do so.

Table 4. $\Delta \ln Z$ for various **Exoretrievals** (left) and **PLATON** (right) models relative to a clear (and flat for **Exoretrievals**’s case) spectrum with the subset of data that included only the Magellan/IMACS and HST/WFC3 data. The retrievals with water and sodium were heavily supported by **Exoretrievals**. Models that included scattering were the most supported with **PLATON**.

Exoretrievals							PLATON	
Model:	flat	H_2O	Na	K	$H_2O + Na$	$H_2O + K + Na$	Model:	
clear	0.0	6.99	−0.39	4.07	12.78	10.94	clear	0.0
scatterers	− − −	5.5	−0.89	3.49	8.78	8.39	scattering	4.54
activity	0.35	5.97	−1.23	4.04	10.65	10.1	activity	0.6
Both	− − −	4.91	−1.92	3.34	9.63	−4.05	Both	4.14

which is in agreement with what **Exoretrievals** found for the FORS2 dataset. That is the slope blue-ward of 500 nm could be explained by either activity or a scattering slope, but neither is required for the data. For the FORS2 dataset the best fit model including activity found $\Delta T = -1040_{-1000}^{+1200}$ and $f = 0.0143_{-0.0089}^{+0.0083}$; the best fit model including scatterers found a scattering slope, α , of $5.7_{-6.0}^{+5.3}$ ($\alpha=4$ is Rayleigh); and the highest evidence model (clear model) obtained a metallicity, $\log_{10}(Z/Z_{\odot})$, of $0.26_{-0.78}^{+0.75}$ dex, C/O of $1.11_{-0.39}^{+0.55}$, $\log_{10}(P_0)$ of $0.3_{-1.3}^{+1.7}$ bars, and T_p of 987_{-52}^{+92} . Contrarily to **PLATON**, the IMACS data obtained a significantly higher evidence ($\Delta \ln Z > 4$) for the models that included scatterers. The retrieved values with IMACS differed from the fit with FORS2 likely because the Na feature was not as prominent in the IMACS data. Thus, the retrieval increases the metallicity ($\log_{10}(Z/Z_{\odot}) = 0.51_{-0.75}^{+0.53}$ dex) and decreases the temperature (T_p of 752_{-94}^{+62} K) to mute the Na feature. In turn, the best retrieved spectrum is overall different from the FORS2 spectrum. Still the retrieved scattering slope of both datasets was consistent with a Rayleigh scattering slope, though not well constrained.

6.2. Combined Transmission Spectrum

The $\Delta \ln Z$ of all models run using the global data against both retrievals is shown in Table 7. When running the retrievals against the combined data, we find a similar trend as that for the individual datasets (aside for IMACS with **PLATON**). That is, a major detection of water and sodium, and tentative signs of a blue-ward slope attributed to stellar activity or a scattering slope.

For **Exoretrievals** the evidence, $\Delta \ln Z = 19.45$, is even stronger than the individual datasets, showing that combining the data does improve the overall detection of the species. The corner plot of the highest-evidence model retrieved by **PLATON** (one with scatters) and **Exoretrievals** (one without activity and scatters but including H_2O and Na) is shown in Figures 7 and 8. Figures 9 and 10 show the global data with over-plotted models that either include stellar activity, a scattering slope, or none (flat and clear) for both retrievals. We elect to use the global transmission spectra which included all optical data to interpret the retrievals and atmosphere of WASP-96b, because the maximum relative retrieved evidence and transmission spectrum precision are higher when including both optical data.

7. RETRIEVAL INTERPRETATION

7.1. Atomic and Molecular Features

The retrieved mixing ratios of sodium ($\log_{10}(Na) = -5.4_{-1.9}^{+2.0}$) and water ($\log_{10}(H_2O) = -4.5 \pm 2.0$) are

in agreement both with what was obtained by Yip et al. 2021 ($\log_{10}(Na) = -3.88_{-0.82}^{+1.05}$ and $\log_{10}(H_2O) = -3.65_{-0.94}^{+0.90}$) and what was obtained by Nikolov et al. 2018 ($\log_{10}(Na) = -5.1_{-0.4}^{+0.6}$). The Na mixing ratios obtained here are consistent with solar abundance ($\log_{10}(Na) = -5.78 \pm 0.03$; Asplund et al. 2021) and WASP-96's stellar abundance (Nikolov et al. 2018). The water abundance is also consistent with water abundances of Jupiter constrained by Juno ($\log_{10}(H_2O) = -2.6_{-0.44}^{+0.27}$; Li et al. 2020). This implies that the formation process for WASP-96b might have been similar to our own Jovians, but that conclusion is limited by the uncertainties in the measured mixing ratios.

Theoretical predictions for clear atmosphere planets predict absorption signatures from the optical alkali features of Na and K (Seager & Sasselov 2000). However, our observations of WASP-96b show no observable evidence of K absorption, even though strong Na I and H_2O features imply WASP-96b has a clear transmission spectrum. There are multiple possibilities as to why potassium was not significantly detected. The most obvious hindrance in detecting K was the gap in the transmission spectrum (759.4–767.2 nm) that was nearly aligned with the center of the most prominent K doublet feature (768.15 nm). Essentially, this only allowed K to be constrained by its wings, which might not be enough even if K is present. The possibility of K being present in the atmosphere is hinted in Figure 9, where **PLATON**'s retrievals by default include K because of imposed equilibrium chemistry and relative abundances determined by metallicity. In those models we see that the transmission spectrum is somewhat consistent with the K doublets' features, where the blue-ward bin in the K wing is within the model's $1-\sigma$ interval and the red-ward bin is not. The fact that the evidences of the **Exoretrievals** models including K are lower than those excluding it is likely only because the data could be explained with or without K, given the gap in the central doublet band. Another possibility is that the potassium is locked away in KCl, which has been suggested to have a highly efficient formation rate in this temperature regime (Gao et al. 2020). Further space-based observations, or ground based high resolution observations will be needed to determine if abundant K absorption is truly present in the atmosphere of WASP-96b.

7.2. Activity and Optical Slope

For the models that included activity, retrieved ΔT temperatures from both retrievals and all datasets were consistent ($< 1-\sigma$) with no active regions ($\Delta T = 0$ K), implying a non-detection of stellar activity. Therefore, stellar photometry (see sec. 5.1 & 5.3), stellar spec-

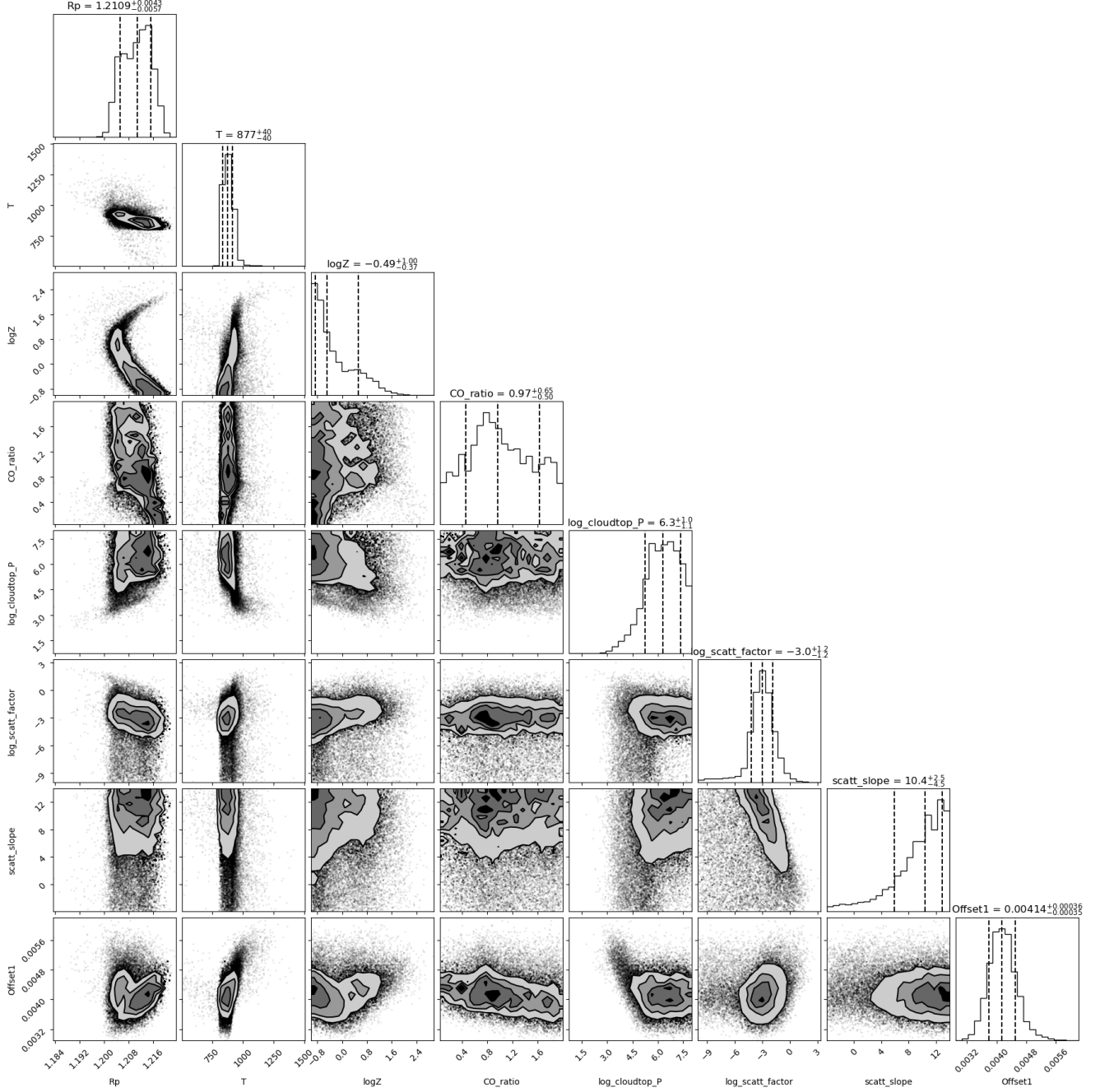


Figure 7. Corner plot of the PLATON best fit retrieval model with, which is run against the combined Magellan/IMACS, VLT/FORS2, and HST/WFC3 data. Its corresponding transmission spectrum is shown in Figure 9 (red model). Vertical dashed lines mark the 16% and 84% quantiles.

troscopy (see sec. 5.2), and the transmission spectrum retrieval analysis all support the idea that WASP-96 has very little activity.

H₂ Rayleigh scattering is expected blue-wards of $\sim 450\text{--}550\text{ nm}$ in a hydrogen dominated atmosphere without high altitude clouds (i.e. Seager & Sasselov 2000; Lecavelier Des Etangs et al. 2008). The fact that we were unable to significantly identify one is likely due

to limitations of the data, given that we only have two and a half broader bins in this wavelength range. The slope could be better constrained with HST/STIS¹² or

¹² G430L has coverage approximately from $0.29\text{--}0.57\text{ }\mu\text{m}$ <https://www.stsci.edu/hst/instrumentation/stis>

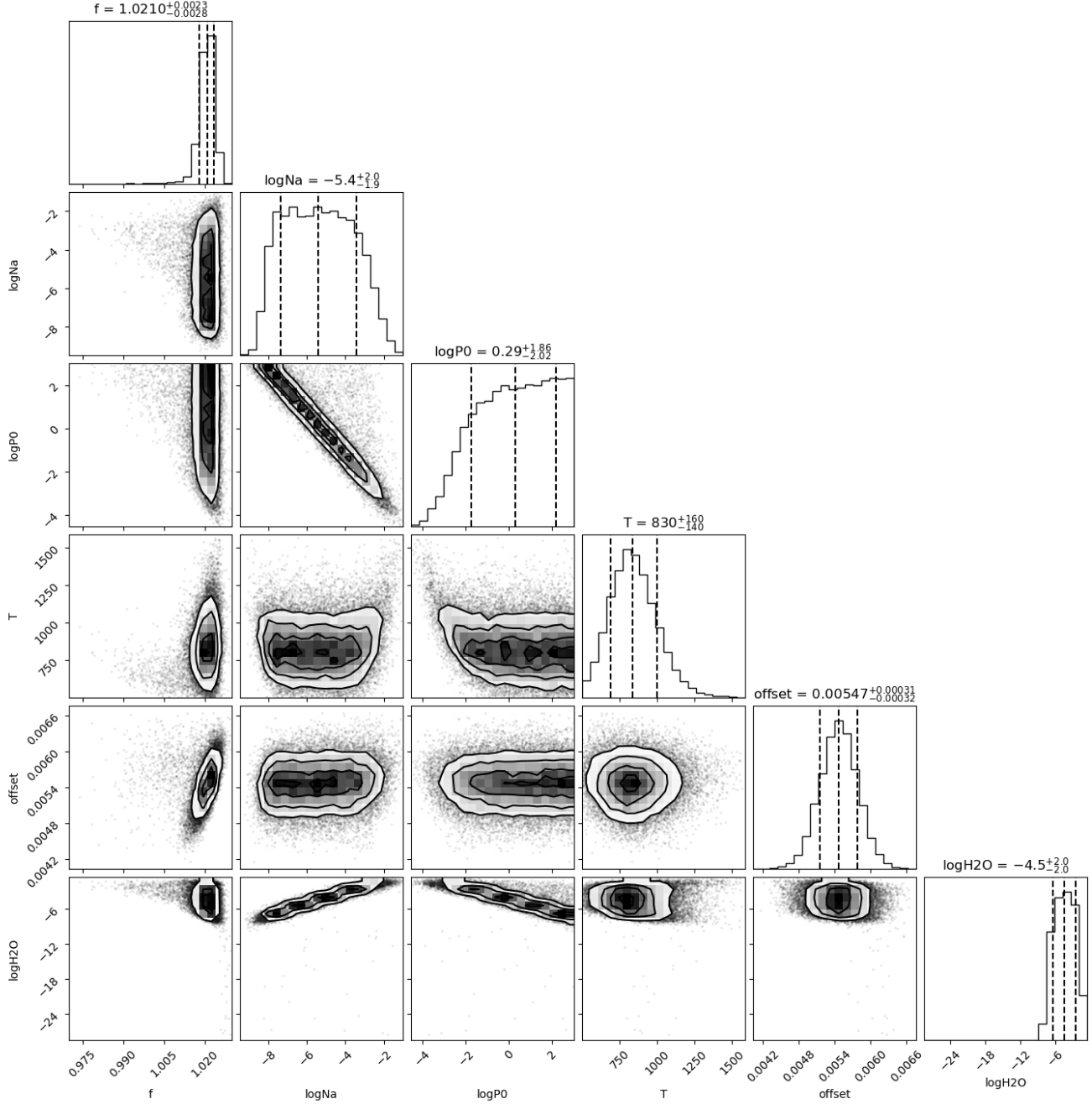


Figure 8. Same as Figure 7, but for *Exoretrievals*, where its corresponding transmission spectrum is shown in Figure 10 (blue colored model).

HST/WFC3/UVIS¹³ observations. This would likely be sufficient to distinguish from stellar activity, because the star is relatively quiet. Therefore, when imposing these constraints, as was done in Section 5.3, the only viable activity features produced are very shallow slopes.

¹³ WFC3/UVIS G280 covers 0.2-0.8 μm and has better throughput in the blue than STIS (Wakeford et al. 2020)

This is outlined in Figures 9 and 10 where the models with activity fit are shown in gray for both figures. Furthermore, the activity of quiet stars, like this one, is dominated by faculae (Reinhold et al. 2019; Rackham et al. 2022), which produces the opposite signal of what is expected of a Rayleigh slope, when the activity regions are unocculted. Meaning that large cold unocculted spots, needed to mimic a Rayleigh slope, would be in direct contradiction to all other observations of

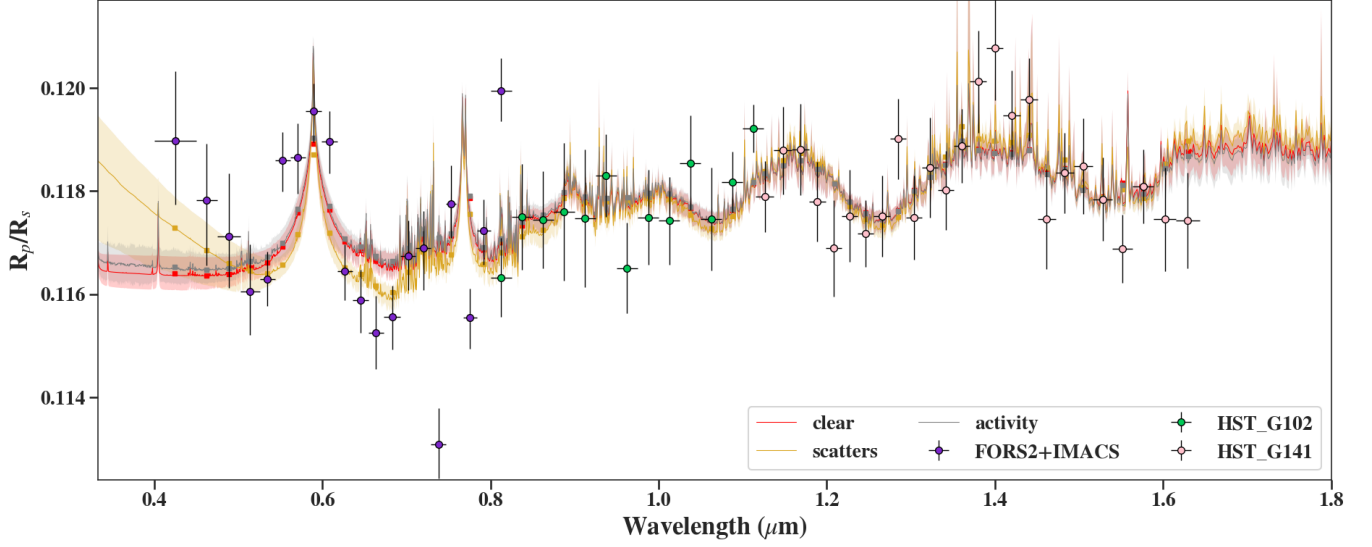


Figure 9. The final transmission spectra of WASP-96b, which include the combined FORS2 and IMACS data (purple) and the G102 (green) and G141 (pink) data both from Yip et al. (2021). Best fit PLATON retrieval models that include stellar activity (grey), scatters (gold), and a clear atmosphere (red) are also plotted, with their 1- σ confidence interval shaded in the same colors. Because for each of the three models, the optical offsets were slightly different, what is shown here is the mean depth where the true offsets were $0.00476^{+0.00040}_{-0.00039}$, $0.00414^{+0.00036}_{-0.00035}$, and $0.00467^{+0.00039}_{-0.00034}$ for the activity, scatters, and clear models, respectively. As can be seen in Table 7 the model with the highest evidence is one with scatters; however, no model has an evidence strong enough to favor it over another.

WASP-96. Thus, it is clear that if a blue-ward scattering slope is found with additional observations, the most viable explanation would be attributing the feature to the planet.

Though the data is not sufficient enough to significantly distinguish between a model with and without a scattering slope, all retrieved scattering slopes were found to be consistent ($< 2\text{-}\sigma$) with a Rayleigh scattering slope. If this can be confirmed the Rayleigh like slope would best be attributed to H_2 scattering.

7.3. Aerosols

The higher reference pressures obtained by PLATON and Exoretrievals (a few to tens of bars) both agree with one another and supports the idea that if WASP-96b hosts thick aerosol layers, they are confined to beneath the top of the atmosphere. The strong water features and broad Na I absorption wings observed also support this conclusion. Additionally, when fitting for aerosols with Exoretrievals the cloud cross section, σ_{cloud} (see Espinoza et al. (2019b) Appendix D) was initially set to be very wide, with log-uniform priors from -80 to 80 for σ_{cloud} . In doing so, we found that across all 3 datasets (i.e. optical data from IMACS, FORS2, and combined) and all iterations of models that include scattering (i.e. no matter which molecules were included or if including activity) the means of σ_{cloud} were nearly the same at ~ -55 . This value is so low it effectively means that the retrievals find no evidence of clouds affecting

the spectra, which is consistent with the strong water and sodium features, and the larger reference pressures.

Aerosols are likely present in the atmosphere of all planets, but when aerosols are not warranted by the retrievals that implies that the aerosols are not thick enough at the high altitudes in which transmission spectroscopy probes to significantly mute the spectral features in the observed wavelengths, and/or they are not significantly present in the terminator. Also, though the retrievals, suggests that data can be explained without thick aerosols, color dependent scatters may still affect the transmission spectra. In particular, the possible Rayleigh scattering slope in the optical cannot be confidently refuted in the combined optical data.

7.4. Temperature and C/O ratio

The terminator temperatures found with PLATON ($T_p = 877 \pm 40$ K) and Exoretrievals ($T_p = 830^{+160}_{-140}$ K) are within agreement of one another and with what Yip et al. (2021) retrieved ($T_p = 954^{+198}_{-195}$ K), given their uncertainties. However, these values are vastly different from the temperature retrieved by Nikolov et al. 2018 ($T_p = 1710^{+150}_{-200}$ K), who used the ATMO models (Amundsen et al. 2014; Goyal et al. 2018) to perform retrieval analysis on their data. Our retrieved temperatures are also far from the 0 albedo equilibrium temperature of 1285 ± 40 K (Hellier et al. 2014). A lower retrieved terminator temperature is often found in the literature and is expected when applying a 1D model

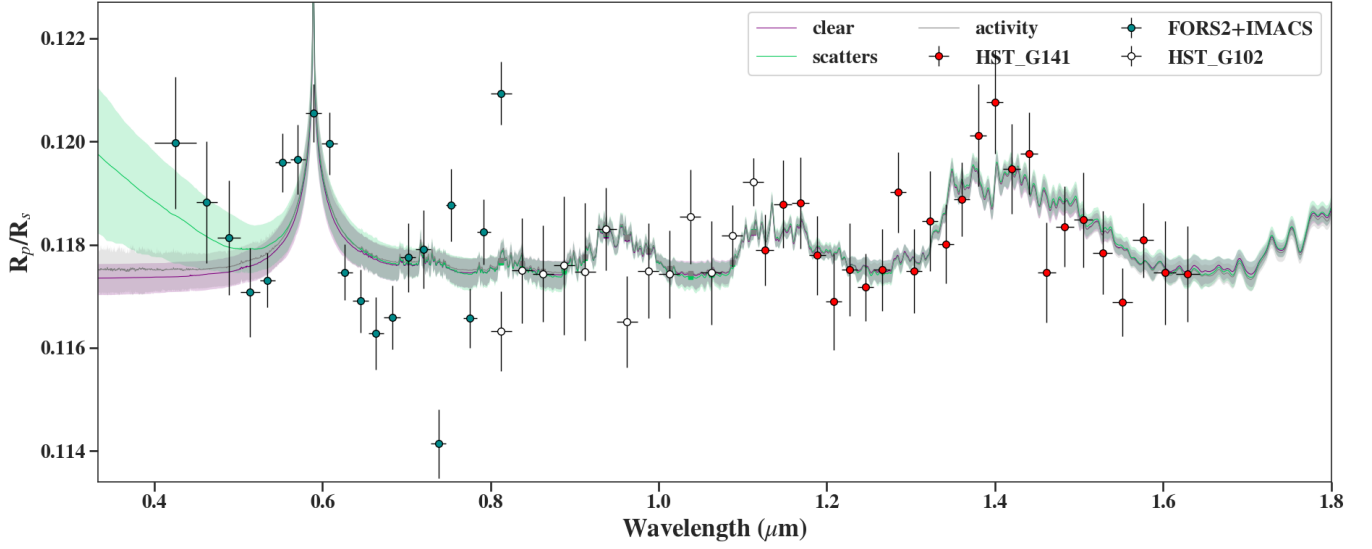


Figure 10. Same as Figure 9, but with Exoretrievals. In this figure the optical (combined FORS2 and IMACS), G102, and G141 observations are cyan, white, and red, respectively. Again, the evidence of each plotted model (activity - gray, scatters - green, and clear - purple) are indistinguishable from each other, but the clear atmosphere has the highest evidence. The offset with each fit were 0.00554 ± 0.00031 , 0.00558 ± 0.00034 , and $0.00547^{+0.00031}_{-0.00032}$ for the activity, scatters, and clear models, respectively.

to probe a 3D atmosphere. 1D models are useful for fitting features found in transmission spectra substantially more quickly than 3D models. Unfortunately, they can artificially shift the retrieved temperature up to hundreds of Kelvin cooler than the true average temperature (MacDonald et al. 2020; Pluriel et al. 2020). Other physical assumptions prescribed in the retrieval frameworks could also contribute to a discrepancy in retrieved temperatures (Welbanks & Madhusudhan 2021).

The only feature in the observed spectrum that could directly constrain C or O was H₂O, thus, the quoted C/O ratios should be taken lightly, given that it is only using the water features and chemical equilibrium constraints to obtain the ratio. Including the two Spitzer/IRAC points centered at 3.6 and 4.5 μm (program ID 14255), as was done by Yip et al. (2021), would include data near carbon bearing features (i.e. CO, CO₂, and CH₄). However, we elected to exclude these points because the two points have larger uncertainties (in wavelength and depth), which would not significantly constrain any of these carbon species, as can be seen in Yip et al. (2021). Given the lack of a constrained C/O ratio, it is hard to ascertain the formation region of WASP-96b, but JWST observations would be able to refine the C/O ratio with higher precision and higher spectral resolution observations in the near- to mid-IR wavelengths. The observed lack of aerosols obscuring features in the optical to near-IR spectrum of WASP-96b makes it an ideal target for such observations, which has the potential to provide key insight of where hot Jupiters formed and when/if they migrated.

8. WASP-96B IN CONTEXT

8.1. Mass-Metallicity Trend

Our metallicity with Platon is consistent with the constraints from Nikolov et al. 2018 ($\log_{10}(Z/Z_{\odot}) = 0.4^{+0.7}_{-0.5}$). Furthermore, it is within 3σ agreement to the solar system mass-metallicity trend (explored for exoplanets by e.g., Wakeford et al. 2018; Alam et al. 2020; Wakeford & Dalba 2020), shown in Figure 11. In this figure we plot the metallicities and masses of the solar system giants and a linear fit of that data in log-log space. We also show planets with metallicities derived from molecular and atomic abundance of one to a few different species.

Looking at all exoplanets in the figure, the trend found for the solar system does not persist among the exoplanet sample. However, given that high-altitude aerosols make it more difficult to accurately determine molecular abundances, we also highlighted the five planets which are thought to have little high-altitude aerosols obscuring their spectra. When only including these planets, four of the five planets (WASP-17b, WASP-62b, WASP-94b, and WASP-96b) are less than 3σ from the predicted values. Though most of the clear atmospheres prove to be consistent with the solar system mass-metallicity trend, it is still hard to claim that we can interpret this as most exoplanets undergo the same formation mechanisms as our solar system for multiple reasons. For one, all three of the consistent metallicities are in similar mass regimes, therefore, giving perspective only on a small fraction of exoplanets. Addi-

Table 5. Same as Table 4 but with the subset of data that included only the VLT/FORS2 and HST/WFC3 data. The retrievals with water and sodium were heavily supported by **Exoretrievals**. There was no model that had high enough evidence to favor it over another with **PLATON**.

Exoretrievals							PLATON	
Model:	flat	H_2O	Na	K	$H_2O + Na$	$H_2O + K + Na$	Model:	
clear	0.0	4.94	0.13	5.81	11.32	10.65	clear	0.0
scatterers	— — —	3.54	−1.41	3.73	9.48	8.97	scattering	−1.18
activity	0.06	4.13	−1.43	4.18	11.38	11.11	activity	−0.18
Both	— — —	3.11	−2.12	3.11	9.13	−4.07	Both	−1.25

Table 6. Parameters obtained by the best-fit retrievals for each data subsets (IMACS with WFC3, FORS2 with WFC3, and combined optical with WFC3). The model which only included water and sodium was the highest-evidence model with **Exoretrievals** for each data subset (the evidence for the model with and without activity was nearly identical in the FORS2 subset). With **PLATON**, the model including scattering was favored with the combined dataset and the IMACS one, but for the FORS2 dataset a featureless model was marginally preferred. Here T_p , P_0 , offset, α , Z/Z_\odot , C/O , and $\log_{10}(H_2O)$, $\log_{10}(Na)$ correspond to planet terminator temperature [K], reference pressure at which the atmosphere is optically thick [bar], offset in transit depth [R_p/R_s], scattering slope (α of 4 is Rayleigh), metallicity of the star relative to solar, carbon-to-oxygen abundance ratio, and log mixing ratios of water and sodium, respectively.

Exoretrievals				PLATON			
	IMACS+WFC3	FORS2+WFC3	combined data		IMACS+WFC3	FORS2+WFC3	combined data
T_p	730^{+180}_{-140}	790^{+220}_{-160}	830^{+160}_{-140}	T_p	752^{+62}_{-94}	987^{+92}_{-52}	877 ± 40
$\log_{10}(P_0)$	$0.64^{+1.63}_{-1.93}$	$0.4^{+1.81}_{-2.17}$	$0.29^{+1.86}_{-2.02}$	$\log_{10}(P_0)$	$1.58^{+0.84}_{-0.97}$	$0.3^{+1.7}_{-1.3}$	$1.3^{+1.0}_{-1.1}$
offset	0.01201 ± 0.0004	$0.00238^{+0.00041}_{-0.00038}$	$0.00547^{+0.00031}_{-0.00032}$	offset	$0.00967^{+0.00034}_{-0.00031}$	$0.00199^{+0.00044}_{-0.00043}$	$0.00414^{+0.00036}_{-0.00035}$
$\log_{10}(H_2O)$	$-3.9^{+1.8}_{-2.0}$	$-4.3^{+1.9}_{-2.1}$	-4.5 ± 2.0	$\log_{10}(Z/Z_\odot)$	$0.51^{+0.53}_{-0.75}$	$0.26^{+0.75}_{-0.78}$	$-0.49^{+1.00}_{-0.37}$
$\log_{10}(Na)$	$-5.5^{+1.8}_{-1.9}$	$-5.0^{+2.0}_{-2.1}$	$-5.4^{+2.0}_{-1.9}$	C/O	$0.69^{+0.72}_{-0.41}$	$1.11^{+0.55}_{-0.39}$	$0.97^{+0.65}_{-0.50}$
				α	$3.7^{+6.3}_{-5.0}$	— — —	$10.4^{+2.5}_{-4.5}$

Table 7. Same as Table 4 but with the dataset that included the combined IMACS, FORS2, and HST data. The retrievals with water and sodium were heavily supported by **Exoretrievals** and no model was preferred with **PLATON**.

Exoretrievals							PLATON	
Model:	flat	H_2O	Na	K	$H_2O + Na$	$H_2O + K + Na$	Model:	
clear	0.0	5.73	−0.56	12.52	19.45	19.11	clear	0.0
scatterers	— — —	6.87	−0.53	11.63	18.35	17.46	scattering	0.8
activity	0.1	5.06	−1.45	12.36	18.33	18.14	activity	−0.28
Both	— — —	4.95	−1.92	10.79	17.62	−4.16	Both	0.55

tionally, most of these metallicities were obtained assuming the abundances of one to a few species can be directly translated to the bulk metallicity of the atmosphere. How far this assumption is skewed from reality is unknown, since interactions among transport, chemistry, and phase changes may mean the elements are not well-mixed in the atmosphere (Zhang 2020). Furthermore, most of the planets in Figure 11 are hot jupiters/neptunes, which are outliers that are not representative to exoplanets in general. For these reasons, and others, there is much headway required in order to obtain a more complete grasp of exoplanet formation mechanisms and trends. Observing more planets like WASP-96b, with relatively clear atmospheres, in many wavelengths and improving our analysis processes around these observations is the best path forward.

Interestingly, though the work from this paper and others (e.g. Alam et al. 2020; Wakeford & Dalba 2020) find no clear trend amongst atmospheric composition and mass, there has been a found mass-metallicity trend in terms of planet bulk composition (Thorngren et al. 2016, , inferred from structure models). Still, much work is needed in order to determine if there truly is or is not an atmospheric metallicity-mass trend before the root of this potential discrepancy can be explored further.

8.2. Correlations to aerosol formation rates

Understanding why WASP-96b is one of the few planets that has an observed transmission spectrum unobscured by aerosols is vital for advances in exoplanetology. This would allow astronomers to a priori determine what key characteristics make an exoplanet transmission spectrum clear and allow for more targeted exo-atmosphere surveys.

Figure 12 puts WASP-96b in a broader context, it was initially used by Stevenson (2016), who proposed a temperature-gravity trend in the formation of high-altitude clouds. They used the H_2O -J index as a proxy for the cloud levels, which inherently assumes a similar absolute water abundance of all hot Jupiters. HAT-P-11b is a prime example of the limitations of using this index as a proxy for cloud formation, where its water feature is extremely strong (2.499 ± 0.505), but its optical spectra revealed it to have a cloudy atmosphere (Chachan et al. 2019). Nonetheless, the H_2O -J index provides an easy index to parameterize cloud levels. Multiple other planets have been added to the original figure (e.g., Alam et al. 2020; Weaver et al. 2021, etc.), and make it clear that the trend does not strictly exist. As seen in our Figure 12, WASP-96b (marked as a star) highlights the lack of an obvious trend even further, where it is near the fitted temperature-log(g)

boundary line but is in fact one of the most clear atmospheres observed to-date. Thus, there is still extended work needed to isolate what causes high-altitude aerosol formation.

9. SUMMARY & CONCLUSION

We observed two transmission spectra of WASP-96b with Magellan/IMACS as part of the ACCESS survey. In the process of analyzing the data, we tested the precisions and accuracies of two commonly used spectroscopic light curve detrending techniques: A) Common mode correction followed by a polynomial fitting (CMC+Poly) and B) a Gaussian processes (GP) routine. Both routines were tested against simulated data, where we find that for data without substantial chromatic systemics the CMC+Poly procedure produces more accurate depths with higher precision. Additionally, we find that neither method (worse for CMC+Poly) was able to consistently reproduce absolute depths. This provided justification of fitting for offsets amongst transmission spectra from different nights and instruments.

The transmission spectrum from IMACS was then added with reanalyzed transmission spectra from FORS2, both of which were reduced using the CMC+Poly routine. The optical data was combined with a previously published HST/WFC3 (G102 and G141) transmission spectrum (Yip et al. 2021), collectively producing a nearly continuous coverage transmission spectrum from 400–1237 nm. This spectrum was run against two retrievals: PLATON and Exoretrievals. Both retrievals found that the terminator of WASP-96b was shrouded by little or no aerosols, as such it is still one of the most clear exo-atmospheres observed. More specifically PLATON found a metallicity, C/O ratio, reference pressure, and terminator temperature of $\log_{10}(Z/Z_{\odot}) = -0.49^{+0.0}_{-0.37}$ dex, $C/O = 0.97^{+0.65}_{-0.50}$, $\log_{10}(P_0) = 1.3^{+1.0}_{-1.1}$ bars, and $T_p = 877 \pm 40$ K, respectively. Exoretrievals found a terminator temperature, reference pressure, and water and sodium mixing ratios of $T_p = 830^{+160}_{-140}$ K, $\log_{10}(P_0) = 0.29^{+1.86}_{-2.02}$ bars, $\log_{10}(H_2O) = -4.5 \pm 2.0$, and $\log_{10}(Na) = -5.4^{+2.0}_{-1.9}$, respectively. With the constraints on stellar activity imposed from photometric monitoring, neither retrieval had strong support for stellar activity explaining the data. Though there is a hint of a slight slope blue-ward of 550 nm, there was not substantial evidence supporting the need for a scattering slope. However, bluer, space-borne observations of the planet could discern if the hint of a blue-ward slope is indeed a true feature.

Finally, in an attempt to put WASP-96b in a broader context, we found that it along with three other clear planets (WASP-62b, WASP-94b, and WASP-17b) are

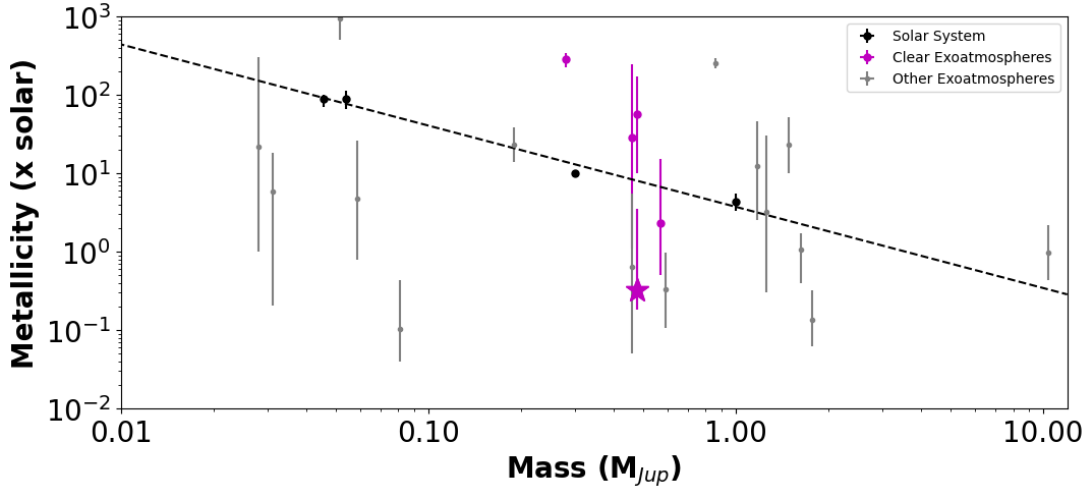


Figure 11. Observed mass-metallicity trend for transiting exoplanets. The bulk of the data was acquired from Wakeford & Dalba (2020)^b, but we added HAT-P-32b (Alam et al. 2020), WASP-17b (PLATON run with data from Sing et al. (2016)), WASP-62b (using Na abundance from Alam et al. (2021) as a proxy), WASP-94b (Ahrer et al. 2022), and WASP-96 (this work, magenta star). The dashed black line corresponds to a linear fit in log-log space to the solar system points (black dots). We highlight the clear planets with magenta and all other planets are gray.

^a<https://stellarplanet.org/science/mass-metallicity/>

^b<https://stellarplanet.org/science/mass-metallicity/>

consistent with the mass-metallicity trend observed in the solar system. However this sample is not complete enough to make overarching claims about the extrasolar giants’ formation mechanisms compared to giant planet formation pathways in the solar system. We also find no clear correlation to what causes the aerosol formation rate in exo-atmospheres, and recommend more in-depth analysis of a higher sample of planets in order to find such a correlation.

The results reported herein benefited from support, collaborations and information exchange within NASA’s Nexus for Exoplanet System Science (NExSS), a research coordination network sponsored by NASA’s Science Mission Directorate. This material is partly based upon work supported by the National Aeronautics and Space Administration under Agreement No. 80NSSC21K0593 for the program “Alien Earths”. This paper includes data gathered with the 6.5 meter Magellan Telescopes located at Las Campanas Observatory, Chile. We thank the staff at the Magellan Telescopes and Las Campanas Observatory for their ongoing input and support to make the ACCESS observations presented in this work possible. This work uses ob-

servations collected at the European Organization for Astronomical Research in the Southern Hemisphere under European Southern Observatory programme 199.C-0467(H). We also appreciate the support from the NSF Graduate Research Fellowship (GRFP), grant number DGE1745303. The computations in this paper were conducted on the Smithsonian High Performance Cluster (SI/HPC), Smithsonian Institution. <https://doi.org/10.25572/SIHPC>.

B.V.R. thanks the Heising-Simons Foundation for support. C.M. thanks Neale Gibson for conversations on marginalization techniques. A.J. acknowledges support from ANID – Millennium Science Initiative – ICN12_009 and from FONDECYT project 1210718.

Software: Astropy (Astropy Collaboration et al. 2013), corner (Foreman-Mackey 2016), Matplotlib (Hunter 2007), NumPy (Oliphant 2006), Multinest (Feroz et al. 2009), PyMultiNest (Buchner et al. 2014), SciPy (Jones et al. 2001), batman (Kreidberg 2015), george (Foreman-Mackey et al. 2014), dynesty (Speagle 2020), PLATON (Zhang et al. 2019), Juliet (Espinoza et al. 2019a)

Facilities: Magellan:Baade, Smithsonian Institution High Performance Cluster (SI/HPC)

REFERENCES

- Ahrer, E., Wheatley, P. J., Kirk, J., et al. 2022, *MNRAS*, 510, 4857
- Alam, M. K., Nikolov, N., López-Morales, M., et al. 2018, *AJ*, 156, 298

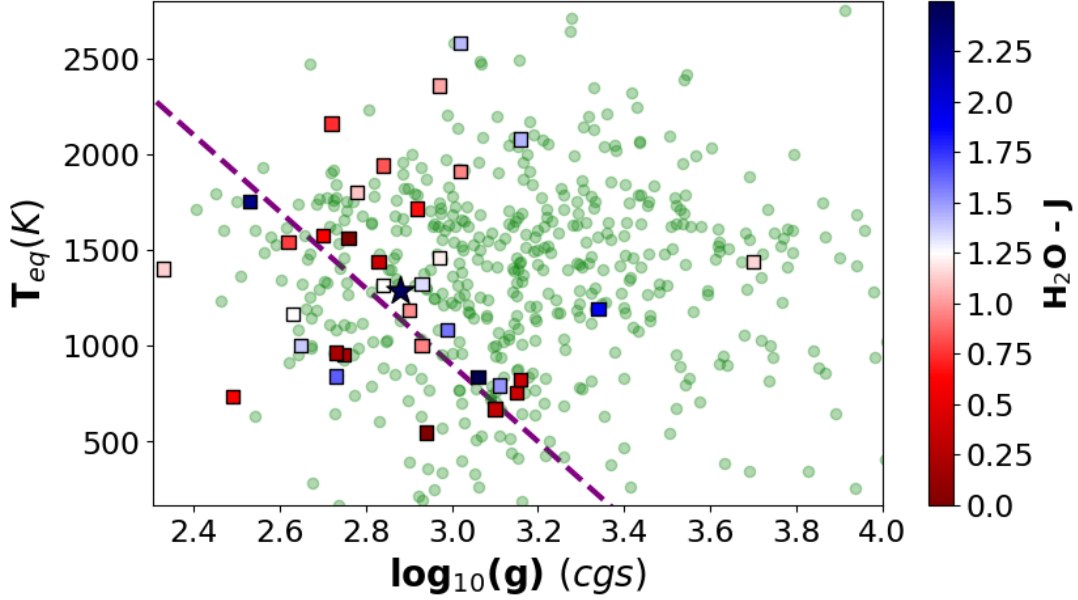


Figure 12. The H₂O-J indices (color coded squares) defined by [Stevenson \(2016\)](#) relative to the planetary surface gravities and equilibrium temperatures. Other planets with surface gravities and effective temperatures obtained from [TEPICat](#) are plotted as green circles for context. We also plot the dividing line in T_{eq} - $\log_{10}(g)$ phase space that [Stevenson \(2016\)](#) proposed delineates between cloudy and clear planets. Where the authors say H₂O-J indices greater than 2 is likely completely clear, and indices less than 1 are greatly obscured by clouds. The only planets with indices greater than 2 are HAT-P-11b (2.5 ± 0.5), WASP-96 (2.4 ± 0.7), and WASP-17b (2.3 ± 0.9). WASP-96 (star) is shown to be one of the clearest observed planets, both through this index and in the optical, yet it sits very close to the dividing line. The data in this table was produced in [Alam et al. \(2020\)](#).

Alam, M. K., López-Morales, M., Nikolov, N., et al. 2020, [AJ](#), 160, 51

Alam, M. K., López-Morales, M., MacDonald, R. J., et al. 2021, [ApJL](#), 906, L10

Amundsen, D. S., Baraffe, I., Tremblin, P., et al. 2014, [A&A](#), 564, A59

Asplund, M., Amarsi, A. M., & Grevesse, N. 2021, [A&A](#), 653, A141

Astropy Collaboration, Robitaille, T. P., Tollerud, E. J., et al. 2013, [A&A](#), 558, A33

Baxter, C., Désert, J.-M., Parmentier, V., et al. 2020, [A&A](#), 639, A36

Benneke, B., & Seager, S. 2013, [ApJ](#), 778, 153

Berdugina, S. V. 2005, [Living Reviews in Solar Physics](#), 2, 8

Berta, Z. K., Charbonneau, D., Bean, J., et al. 2011, [ApJ](#), 736, 12

Bixel, A., Rackham, B. V., Apai, D., et al. 2019, [AJ](#), 157, 68

Buchner, J., Georgakakis, A., Nandra, K., et al. 2014, [A&A](#), 564, A125

Carter, A. L., Nikolov, N., Sing, D. K., et al. 2020, [MNRAS](#), 494, 5449

Chachan, Y., Knutson, H. A., Gao, P., et al. 2019, [AJ](#), 158, 244

Claret, A., Hauschildt, P. H., & Witte, S. 2013, [A&A](#), 552, A16

Diamond-Lowe, H., Berta-Thompson, Z., Charbonneau, D., & Kempton, E. M. R. 2018, [AJ](#), 156, 42

Dressler, A., Bigelow, B., Hare, T., et al. 2011, [PASP](#), 123, 288

Dymont, A. H., Yu, X., Ohno, K., Zhang, X., & Fortney, J. J. 2021, arXiv e-prints, arXiv:2112.06173

Espinoza, N. 2017, PhD thesis, Pontificia Universidad Católica de Chile

Espinoza, N., Kossakowski, D., & Brahm, R. 2019a, [MNRAS](#), 490, 2262

Espinoza, N., Rackham, B. V., Jordán, A., et al. 2019b, [MNRAS](#), 482, 2065

Evans, T. M., Sing, D. K., Kataria, T., et al. 2017, [Nature](#), 548, 58

Evans, T. M., Sing, D. K., Goyal, J. M., et al. 2018, [AJ](#), 156, 283

Feroz, F., Hobson, M. P., & Bridges, M. 2009, [MNRAS](#), 398, 1601

Fischer, P. D., Knutson, H. A., Sing, D. K., et al. 2016, [ApJ](#), 827, 19

Foreman-Mackey, D. 2016, [The Journal of Open Source Software](#), 24

- Foreman-Mackey, D., Hoyer, S., Bernhard, J., & Angus, R. 2014, *George: George* (V0.2.0)
- Fromang, S., Leconte, J., & Heng, K. 2016, *A&A*, **591**, A144
- Fu, G., Deming, D., Knutson, H., et al. 2017, *ApJL*, **847**, L22
- Gandhi, S., & Madhusudhan, N. 2019, *MNRAS*, **485**, 5817
- Gao, P., Thorngren, D. P., Lee, E. K. H., et al. 2020, *Nature Astronomy*, **4**, 951
- Gibson, N. P. 2014, *Monthly Notices of the Royal Astronomical Society*, **445**, 3401
- Gibson, N. P., Aigrain, S., Barstow, J. K., et al. 2013, *MNRAS*, **428**, 3680
- Gibson, N. P., Aigrain, S., Roberts, S., et al. 2012, *MNRAS*, **419**, 2683
- Gibson, N. P., de Mooij, E. J. W., Evans, T. M., et al. 2019, *MNRAS*, **482**, 606
- Gibson, N. P., Nikolov, N., Sing, D. K., et al. 2017, *MNRAS*, **467**, 4591
- Goyal, J. M., Mayne, N., Sing, D. K., et al. 2018, *MNRAS*, **474**, 5158
- Hellier, C., Anderson, D. R., Collier Cameron, A., et al. 2014, *MNRAS*, **440**, 1982
- Heng, K. 2016, *ApJL*, **826**, L16
- Hirano, T., Sanchis-Ojeda, R., Takeda, Y., et al. 2012, *ApJ*, **756**, 66
- Hunter, J. D. 2007, *Computing In Science & Engineering*, **9**, 90
- Jenkins, J. M., Twicken, J. D., McCauliff, S., et al. 2016, in *Society of Photo-Optical Instrumentation Engineers (SPIE) Conference Series*, Vol. 9913, *Software and Cyberinfrastructure for Astronomy IV*, ed. G. Chiozzi & J. C. Guzman, 99133E
- Jones, E., Oliphant, T., Peterson, P., et al. 2001, *SciPy: Open source scientific tools for Python*
- Jordán, A., Espinoza, N., Rabus, M., et al. 2013, *ApJ*, **778**, 184
- Kipping, D. M. 2012, *Monthly Notices of the Royal Astronomical Society*, **427**, 2487
- Kipping, D. M. 2013, *MNRAS*, **435**, 2152
- Kirk, J., López-Morales, M., Wheatley, P. J., et al. 2019, *AJ*, **158**, 144
- Kirk, J., Rackham, B. V., MacDonald, R. J., et al. 2021, *AJ*, **162**, 34
- Kochanek, C. S., Shappee, B. J., Stanek, K. Z., et al. 2017, *PASP*, **129**, 104502
- Komacek, T. D., Showman, A. P., & Parmentier, V. 2019, *ApJ*, **881**, 152
- Kreidberg, L. 2015, *PASP*, **127**, 1161
- Lecavelier Des Etangs, A., Pont, F., Vidal-Madjar, A., & Sing, D. 2008, *A&A*, **481**, L83
- Li, C., Ingersoll, A., Bolton, S., et al. 2020, *Nature Astronomy*, **4**, 609
- Lomb, N. R. 1976, *Ap&SS*, **39**, 447
- MacDonald, R. J., Goyal, J. M., & Lewis, N. K. 2020, *ApJL*, **893**, L43
- Marsh, T. R. 1989, *PASP*, **101**, 1032
- McGruder, C. D., López-Morales, M., Espinoza, N., et al. 2020, *AJ*, **160**, 230
- Middelkoop, F. 1981, *A&A*, **101**, 295
- Moses, J. I., Madhusudhan, N., Visscher, C., & Freedman, R. S. 2013, *ApJ*, **763**, 25
- Moses, J. I., Visscher, C., Fortney, J. J., et al. 2011, *ApJ*, **737**, 15
- Newton, E. R., Mondrik, N., Irwin, J., Winters, J. G., & Charbonneau, D. 2018, *AJ*, **156**, 217
- Nikolov, N., Sing, D. K., Gibson, N. P., et al. 2016, *ApJ*, **832**, 191
- Nikolov, N., Sing, D. K., Fortney, J. J., et al. 2018, *Nature*, **557**, 526
- Noyes, R. W., Hartmann, L. W., Baliunas, S. L., Duncan, D. K., & Vaughan, A. H. 1984, *ApJ*, **279**, 763
- Oliphant, T. E. 2006, *Guide to NumPy*, Provo, UT
- Oshagh, M., Santos, N. C., Ehrenreich, D., et al. 2014, *A&A*, **568**, A99
- Pallavicini, R., Golub, L., Rosner, R., et al. 1981, *ApJ*, **248**, 279
- Panwar, V., Désert, J.-M., Todorov, K. O., et al. 2022, *MNRAS*, **510**, 3236
- Parviainen, H., & Aigrain, S. 2015, *MNRAS*, **453**, 3821
- Pluriel, W., Zingales, T., Leconte, J., & Parmentier, V. 2020, *A&A*, **636**, A66
- Pont, F., Knutson, H., Gilliland, R. L., Moutou, C., & Charbonneau, D. 2008, *MNRAS*, **385**, 109
- Pont, F., Sing, D. K., Gibson, N. P., et al. 2013, *MNRAS*, **432**, 2917
- Powell, D. 2021, PhD thesis, University of California, Santa Cruz
- Rackham, B., Espinoza, N., Apai, D., et al. 2017, *ApJ*, **834**, 151
- Rackham, B. V., Apai, D., & Giampapa, M. S. 2019, *AJ*, **157**, 96
- Rackham, B. V., Espinoza, N., Berdyugina, S. V., et al. 2022, arXiv e-prints, arXiv:2201.09905
- Reiners, A., Schüssler, M., & Passegger, V. M. 2014, *ApJ*, **794**, 144
- Reinhold, T., Bell, K. J., Kuzlewicz, J., Hekker, S., & Shapiro, A. I. 2019, *A&A*, **621**, A21

- Ricker, G. R., Winn, J. N., Vanderspek, R., et al. 2014, in [Proc. SPIE, Vol. 9143, Space Telescopes and Instrumentation 2014: Optical, Infrared, and Millimeter Wave](#), 914320
- Rothman, L. S., Gordon, I. E., Barber, R. J., et al. 2010, [JQSRT](#), **111**, 2139
- Rothman, L. S., Gordon, I. E., Babikov, Y., et al. 2013, [JQSRT](#), **130**, 4
- Roudier, G. M., Swain, M. R., Gudipati, M. S., et al. 2021, [AJ](#), **162**, 37
- Seager, S., & Sasselov, D. D. 2000, [ApJ](#), **537**, 916
- Sedaghati, E., Boffin, H. M. J., MacDonald, R. J., et al. 2017, [Nature](#), **549**, 238
- Sing, D. K., Wakeford, H. R., Showman, A. P., et al. 2015, [MNRAS](#), **446**, 2428
- Sing, D. K., Fortney, J. J., Nikolov, N., et al. 2016, [Nature](#), **529**, 59
- Sing, D. K., Lavvas, P., Ballester, G. E., et al. 2019, [AJ](#), **158**, 91
- Southworth, J., Mancini, L., Madhusudhan, N., et al. 2017, [AJ](#), **153**, 191
- Speagle, J. S. 2020, [MNRAS](#), **493**, 3132
- Stevenson, K. B. 2016, [ApJL](#), **817**, L16
- Tennyson, J., Yurchenko, S. N., Al-Refaie, A. F., et al. 2016, [Journal of Molecular Spectroscopy](#), **327**, 73
- Thorngren, D. P., Fortney, J. J., Murray-Clay, R. A., & Lopez, E. D. 2016, [ApJ](#), **831**, 64
- Trotta, R. 2008, [Contemporary Physics](#), **49**, 71
- Tsiaras, A., Waldmann, I. P., Rocchetto, M., et al. 2016, [ApJ](#), **832**, 202
- Tsiaras, A., Waldmann, I. P., Zingales, T., et al. 2018, [AJ](#), **155**, 156
- Vaughan, A. H., & Preston, G. W. 1980, [PASP](#), **92**, 385
- Venot, O., Hébrard, E., Agúndez, M., et al. 2012, [A&A](#), **546**, A43
- Wakeford, H. R., & Dalba, P. A. 2020, [Philosophical Transactions of the Royal Society of London Series A](#), **378**, 20200054
- Wakeford, H. R., Wilson, T. J., Stevenson, K. B., & Lewis, N. K. 2019a, [Research Notes of the American Astronomical Society](#), **3**, 7
- Wakeford, H. R., Sing, D. K., Deming, D., et al. 2018, [AJ](#), **155**, 29
- Wakeford, H. R., Lewis, N. K., Fowler, J., et al. 2019b, [AJ](#), **157**, 11
- Wakeford, H. R., Sing, D. K., Stevenson, K. B., et al. 2020, [AJ](#), **159**, 204
- Weaver, I. C., López-Morales, M., Espinoza, N., et al. 2020, [AJ](#), **159**, 13
- Weaver, I. C., López-Morales, M., Alam, M. K., et al. 2021, [AJ](#), **161**, 278
- Welbanks, L., & Madhusudhan, N. 2021, arXiv e-prints, arXiv:2112.09125
- Winn, J. N., Holman, M. J., Torres, G., et al. 2008, [ApJ](#), **683**, 1076
- Yan, F., Espinoza, N., Molaverdikhani, K., et al. 2020, [A&A](#), **642**, A98
- Yip, K. H., Changeat, Q., Edwards, B., et al. 2021, [AJ](#), **161**, 4
- Yurchenko, S. N., Tennyson, J., Barber, R. J., & Thiel, W. 2013, [Journal of Molecular Spectroscopy](#), **291**, 69
- Zacharias, N., Finch, C. T., Girard, T. M., et al. 2013, [AJ](#), **145**, 44
- Zhang, M., Chachan, Y., Kempton, E. M. R., & Knutson, H. A. 2019, [PASP](#), **131**, 034501
- Zhang, X. 2020, [Research in Astronomy and Astrophysics](#), **20**, 099

APPENDIX

A. SECOND ORDER CONTAMINATION

As mentioned in Section 2.2, we did not use a blocking filter during the UT170804 transit, but we added the GG495 blocking filter in the UT171108 observations after we learned from other ACCESS observations that second order light introduces contamination in some cases.

To check for possible contamination in the UT170804 observation, we modeled its effect by convolving the unfiltered stellar spectra, which inherently is a convolution of the instrument’s throughput and WASP-96’s stellar spectra, with the G495 filter’s throughput. This gave us the spectral profile of the UT170804 observation, if the G495 filter had been added, but with any second order light still present. Then we modeled the normalized continuum of this light curve against the normalized continuum of the UT171108 observations light curve. Because we assumed that the only difference between both continuum structures should be from the 2nd order light, we used the ratio of the two continua as a correction term for the second order light. This process is illustrated in Figure 13. We applied this correction method to each comparison star and WASP-96 spectrum observed on UT170804 (the exact correction term is unique per spectrum) to determine the effect of the second order light. We then used both the corrected and uncorrected spectra to produce a white-light curve and binned light curves, which are constructed by integrating either all wavelengths of light (white-light) or specific band passes (binned) in a given spectrum, and plotting each integrated spectral counts relative to time. Next, we compared the final white-light and binned transits with and without the correction, and found an insignificant difference between the two. This is likely, because the relative effect of the second order light is negated when dividing by the comparison stars (or using a PCA correction with the comparison stars). Given that the correction had minimal effects, in our final analysis we used the uncorrected spectra.

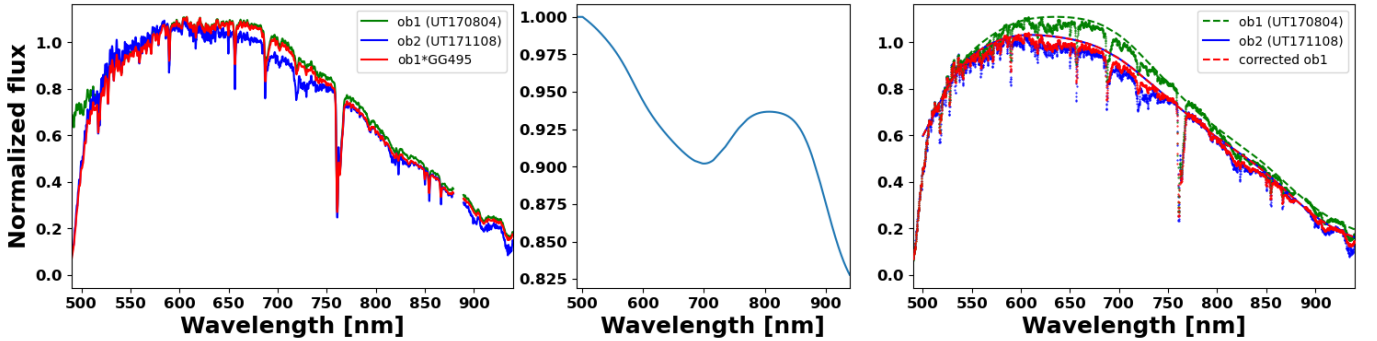


Figure 13. The process used to correct for second order light. The left panel shows the normalized IMACS observations taken on UT170804, which had no filter (red); UT170804 convolved with the GG495 transmission profile (green); and UT171108, which had the GG495 filter (blue). The middle panel shows the normalized second order light correction, determined by dividing the filter convolved first night (green) by the second night (blue). The right panel shows normalized UT170804 (red), UT170804 convolved with the GG495 profile and corrected for second order light (green), and UT171108 (blue). Dotted lines of each spectra’s modeled continua is overlayed in the same respective colors as their spectra. These steps are also applied to each comparison so every spectrum is corrected from second order light.

B. DETRENDING ROUTINES

B.1. *Principle Component Analysis (PCA) and Gaussian Processes (GP)*

The PCA+GP routine we used has been implemented often in recent years (Weaver et al. 2020; Yan et al. 2020; McGruder et al. 2020; Weaver et al. 2021), but we outline it here. We first model out common systematics found in all the comparison stars by performing singular value decomposition on a matrix composed of comparison light curves ($L_k(t)$) in the form:

$$L_k(t) = \sum_{i=1}^K A_{k,i} s_i(t), \quad (\text{B1})$$

where $s_i(t)$ is a set of signals representing the systematics affecting a given light curve and $A_{k,i}$ is the weight for each of those signals. This allows us to identify the principal components (i.e. PCA) of the light curve, which is driven by systematics. This is used rather than just dividing the target by the sum or mean light curve of the comparison stars, because when doing that you combine systematics that are unique to a specific star, instead of isolating which systematics persist amongst all stars. Therefore, this method is less likely to incorrectly divide out systematics in the comparison star that were not present in the target star.

To model out systematics unique to the target’s light curve we used a Gaussian process (GP) regression with a joint probability distribution of the form $\mathcal{N}[0, \Sigma]$, where the covariance function (Σ) is defined as $K_{SE}(x_i, x_j) + \sigma_w^2 \delta_{i,j}$. Here, σ_w^2 and $\delta_{i,j}$ are a jitter term and the Kroenecker delta function, respectively. $K_{SE}(x_i, x_j)$ is a multidimensional squared-exponential kernel of the form:

$$K_{SE}(x_i, x_j) = \sigma_{GP}^2 \exp \left(- \sum_{d=1}^D \alpha_d (x_{d,i} - x_{d,j})^2 \right), \quad (\text{B2})$$

where σ_{GP}^2 is the amplitude of the GP and α_d are the inverse (squared) length-scales of each components of the GP. The priors on the jitter term and σ_{GP}^2 were both log-uniform, where the jitter term ranged from 0.01 to 100 ppm and σ_{GP}^2 from 0.01 to 100 mmag. The prior on each α_d was an exponential function, similar to what was done by Gibson et al. (2017) and Evans et al. (2018).

In the above equations index i denotes each time-stamp and d corresponds to a set of different time-dependent external (auxiliary) parameters used. For the Magellan/IMACS transits these auxiliary parameters were variation of air mass, full-width at half-maximum (FWHM) of the spectra, mean sky flux, position of the central pixel trace (perpendicular to the dispersion axis), and drift of the wavelength solution. For the VLT/FORS2 transits they were dispersion and cross-dispersion drift, variation of the FWHM of the spectra, air mass, mean sky flux, and change in rotator angle.

The PCA and GP components were combined using the following equation:

$$M_k(t) = c_k + \sum_{i=1}^{N_k} A_{k,i} s_i(t) - 2.51 * \log_{10} T(t|\phi) + \epsilon, \quad (\text{B3})$$

where $M_k(t)$ is the (mean-subtracted) magnitude of the target star in the k^{th} model, c_k is a magnitude offset, N_k is the number of PCA signals $s_i(t)$, $A_{k,i}$ is the weight for each signal in each models, $T(t|\phi)$ is the transit model with parameters ϕ ¹⁴, and ϵ our GP component¹⁵.

We used Buchner et al. (2014)’s Nested sampling routine, **PyMultiNest** (a python wrapper of **MultiNest**, Feroz et al. 2009), to explore the posteriors of our PCA+GP models. Because Nested sampling provides Bayesian evidences of models, we used those evidences as weights to combine posterior distributions of each $M_k(t)$ model in a technique called Bayesian Model Averaging (BMA, Gibson 2014).

In the limiting case where there is only one comparison star, the PCA portion of the routine cannot be performed. In that case equation B3 becomes

$$M(t) = c_0 + A * m_c(t) - 2.51 * \log_{10} T(t|\phi) + \epsilon, \quad (\text{B4})$$

where $M(t)$, $T(t|\phi)$, c_0 , and ϵ are the same as $M_k(t)$, $T(t|\phi)$, c_k , and ϵ from equation B3, but without summing over different N_k PCA signals. A is now a weight for the mean-subtracted comparison star magnitude, m_c . This equation is what was used by Yan et al. (2020), because they only had one comparison star.

When this detrending routine can be used to its fullest (i.e. with multiple comparison stars) it is referred as “PCA+GP.” In the case when there is only one comparison star, like in the FORS2 data, it is referred to as a “GP” routine. As discussed in Section 3.3 and Appendix E, the synthetic data only had one comparison star, so we in fact are comparing the GP and CMC+Poly routines in that analysis.

This general procedure can be used to detrend both the white-light curves and the binned-light curves. When producing the binned-light curves solely with PCA+GP we first used this method on the white-light data, then fixed

¹⁴ We used the Python package **batman** (Kreidberg 2015) to produce the analytic transit model.

¹⁵ We used **george** (Foreman-Mackey et al. 2014) to evaluate the GP marginalized likelihoods

all parameters based on the PCA+GP white-light fit (aside from q_1 , q_2 , and R_p/R_s), then ran the PCA+GP routine against the binned-light curves. When producing the binned-light curves with the CMC+Poly routine we again used the PCA+GP method on the white-light data, used that white-light fit to obtain the CMC term, fixed all binned-light curve parameters based on the PCA+GP white-light fit (aside from q_1 , q_2 , and R_p/R_s), and ran the CMC+Poly routine (see sec. B.2).

B.2. Common Mode Correction (CMC)

The general process in CMC is to first produce a partially detrended white-light curve, where the larger systematics common to the target and the comparison(s) are removed. Two common ways to do this is either by dividing the light curve of the target by the light curve of the star(s) or with PCA. Next, a best fit transit model for the light curve is found using a routine that fits for both a transit and additional systematics (e.g. GPs). This transit model is divided by the uncorrected white-light curve to produce a constant systematic correction term (common mode). The correction term is then used for each individual bin, because the systematics are expected to be relatively consistent throughout each spectral band pass. After the common systematics are removed, each bin has an additional detrending routine (e.g. GPs or polynomial correction) to correct for any residual chromatic systematics. Doing this technique has proven to produce relatively high precision (though accuracy was not tested) for retrieved transit depths of each band pass (Gibson et al. 2013; Nikolov et al. 2016; Gibson et al. 2017; Nikolov et al. 2018; Carter et al. 2020).

Our best fit white-light curve transit model (used for the common mode term) is obtained with the same steps of Appendix B.1. After the common mode correction is applied we fit the remaining systematics using 1st and 2nd order polynomial fits of all external parameters. We individually explore the posterior space of all possible combinations of systematic corrections. This means for each bin, including a fit without external parameters (just a single constant coefficient), 729 and 243 models were fit for the IMACS and FORS2 data, respectively. The posterior space was explored in three steps: first, we fit for just the polynomial systematic coefficients on the out-of-transit data using `scipy.optimize.minimize` (Jones et al. 2001) with the 'Powell' method, coefficient bounds of -5 to 5, and initial points of 0. Then we use the found coefficients as the initial start points of another `scipy.optimize.minimize` run which includes the in transit data and a transit model fit. Lastly, we use `PyMultiNest` as our final posterior exploration where the transit parameters found with `scipy` were used as priors on the mean value, while maintaining the prior bounds (see Sec. 3.1), and the found polynomial coefficients were used as the mean values for a normal prior distributions with a standard deviations of 0.05. Again, we used BMA to best combine posteriors from all explored posterior spaces. For the fits we held t_0 fixed to what the white-light curve fit found, thus, the only transit parameters fit were the LD parameters and R_p/R_s . There are differences in how this technique is implemented compared to Nikolov et al. (2018)'s method; however, it produces a nearly identical transmission spectrum, as shown in Figure 14.

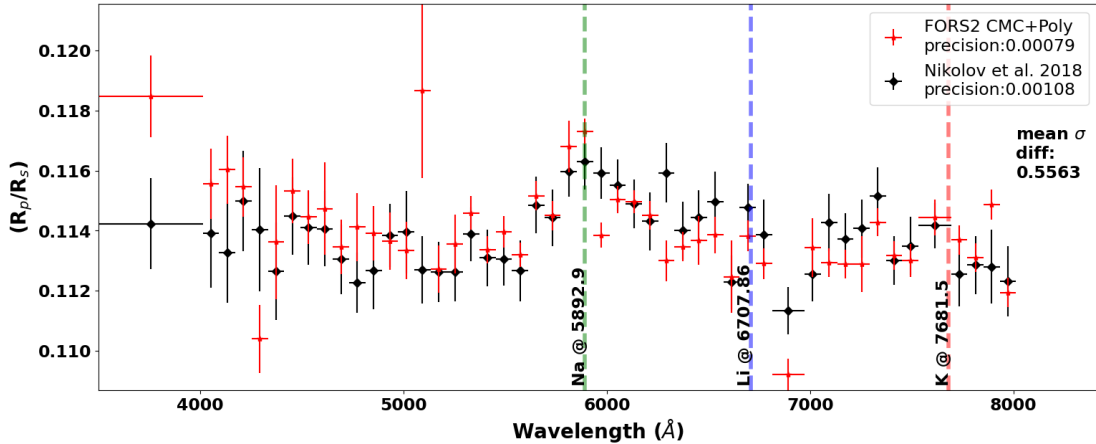


Figure 14. The original transmission spectrum of WASP-96b analyzed by Nikolov et al. (2018) (black), and a re-reduction of the same data (VLT/FORS2) with the same binning scheme using our CMC+Poly analysis discussed in section B.2. The two analyses produce similar mean R_p/R_s precisions (0.00108 for the original and 0.0079 our reanalysis) and have an average difference of depth of only 0.56σ , suggesting strong agreement of the two data. An offset is applied so the means of both datasets are the same.

C. DETRENDING PLOTS

D. LIGHT CURVES

For each bin we estimated the theoretical photon noise precision σ_w . This was calculated by taking the mean counts (per star) over each exposure, summing all the counts (N) in a given bin, and using \sqrt{N} to estimate the shot noise for each star. The error of each star was propagated where the final (uncorrected) transit light curve was produced by dividing WASP-96's flux by the sum of the comparison stars' flux.

We also estimate the noise of the corrected binned light curves. This was done with two approaches. First we calculate the root mean squared (r.m.s.) of the residuals. To also include an estimate that is not dependent on the best fit transit model, we take the standard deviation of the out-of-transit data. Both methods produced similar precisions and we use the higher of the two for our estimates of the the corrected light curve precision.

We quantify the red noise by taking the ratio of the detrended light curve's noise level and the theoretical photon noise. We call this ratio β , as it is similar to the β term used by Winn et al. (2008) (though derived differently). The average β is 1.122, 1.671, 1.089, and 1.528 for each night in chronological order. Their corresponding R_p/R_s uncertainties are 0.001262, 0.002284, 0.000935, and 0.001485, correlated to the total light curve precision (red and white noise) but overall determined by how well the posterior space can be constrained, given the data.

Table 8. Combined Magellan/IMACS (UT170804 and UT171108) optical transmission spectrum (R_p/R_s), combined VLT/FORS2 (UT170729 and UT170822) optical transmission spectrum, and global combined optical spectrum (all four transits). The data were produced implementing the reduction and detrending processes discussed in Section 4. These depths are offset so the mean depth is 0.1158.

Wavelength (Å)	Magellan/IMACS	VLT/FORS2	Global
4000.0 – 4500.0	— — —	$0.1173^{+0.0014}_{-0.0013}$	$0.1177^{+0.0014}_{-0.0013}$
4500.0 – 4750.0	— — —	$0.1161^{+0.0011}_{-0.0013}$	$0.1165^{+0.0011}_{-0.0013}$
4750.0 – 5025.0	$0.1165^{+0.0036}_{-0.0043}$	$0.1153^{+0.0011}_{-0.0013}$	$0.1158^{+0.0013}_{-0.001}$
5025.0 – 5255.0	$0.1143^{+0.0014}_{-0.0015}$	$0.1149^{+0.0011}_{-0.0013}$	0.1147 ± 0.0009
5255.0 – 5435.0	$0.1138^{+0.0011}_{-0.001}$	0.1153 ± 0.0006	$0.1149^{+0.0006}_{-0.0005}$
5435.0 – 5615.0	$0.1207^{+0.0011}_{-0.0012}$	0.1158 ± 0.0007	0.1173 ± 0.0006
5615.0 – 5800.5	$0.1185^{+0.0023}_{-0.002}$	$0.1169^{+0.0007}_{-0.0008}$	0.1174 ± 0.0007
5800.5 – 5985.5	0.1184 ± 0.0009	$0.1185^{+0.0007}_{-0.0009}$	$0.1183^{+0.0005}_{-0.0006}$
5985.5 – 6175.0	$0.1186^{+0.0011}_{-0.001}$	0.1173 ± 0.0008	0.1177 ± 0.0006
6175.0 – 6360.0	0.1139 ± 0.0009	$0.1162^{+0.0008}_{-0.0007}$	$0.1151^{+0.0005}_{-0.0006}$
6360.0 – 6545.0	0.1139 ± 0.0009	$0.1156^{+0.001}_{-0.0008}$	$0.1145^{+0.0006}_{-0.0007}$
6545.0 – 6730.0	$0.1135^{+0.001}_{-0.0009}$	$0.1151^{+0.0012}_{-0.0011}$	0.1139 ± 0.0007
6730.0 – 6930.0	0.1141 ± 0.0009	$0.1147^{+0.001}_{-0.0009}$	$0.1142^{+0.0006}_{-0.0007}$
6930.0 – 7110.0	$0.1155^{+0.0015}_{-0.0018}$	$0.115^{+0.0007}_{-0.0008}$	0.1154 ± 0.0007
7110.0 – 7290.0	$0.1167^{+0.0014}_{-0.0015}$	$0.115^{+0.001}_{-0.0009}$	$0.1156^{+0.0007}_{-0.0009}$
7290.0 – 7470.0	$0.1073^{+0.0012}_{-0.001}$	$0.1154^{+0.001}_{-0.0009}$	0.1116 ± 0.0007
7470.0 – 7594.0	$0.1168^{+0.0012}_{-0.0011}$	$0.1161^{+0.0009}_{-0.001}$	$0.1165^{+0.0008}_{-0.0007}$
7672.0 – 7836.0	$0.1134^{+0.0008}_{-0.0009}$	$0.1152^{+0.0009}_{-0.0008}$	0.1142 ± 0.0006
7836.0 – 8000.0	0.116 ± 0.0009	$0.1163^{+0.001}_{-0.0009}$	$0.1159^{+0.0006}_{-0.0007}$
8000.0 – 8250.0	0.1225 ± 0.0008	$0.114^{+0.001}_{-0.0011}$	$0.1187^{+0.0007}_{-0.0006}$

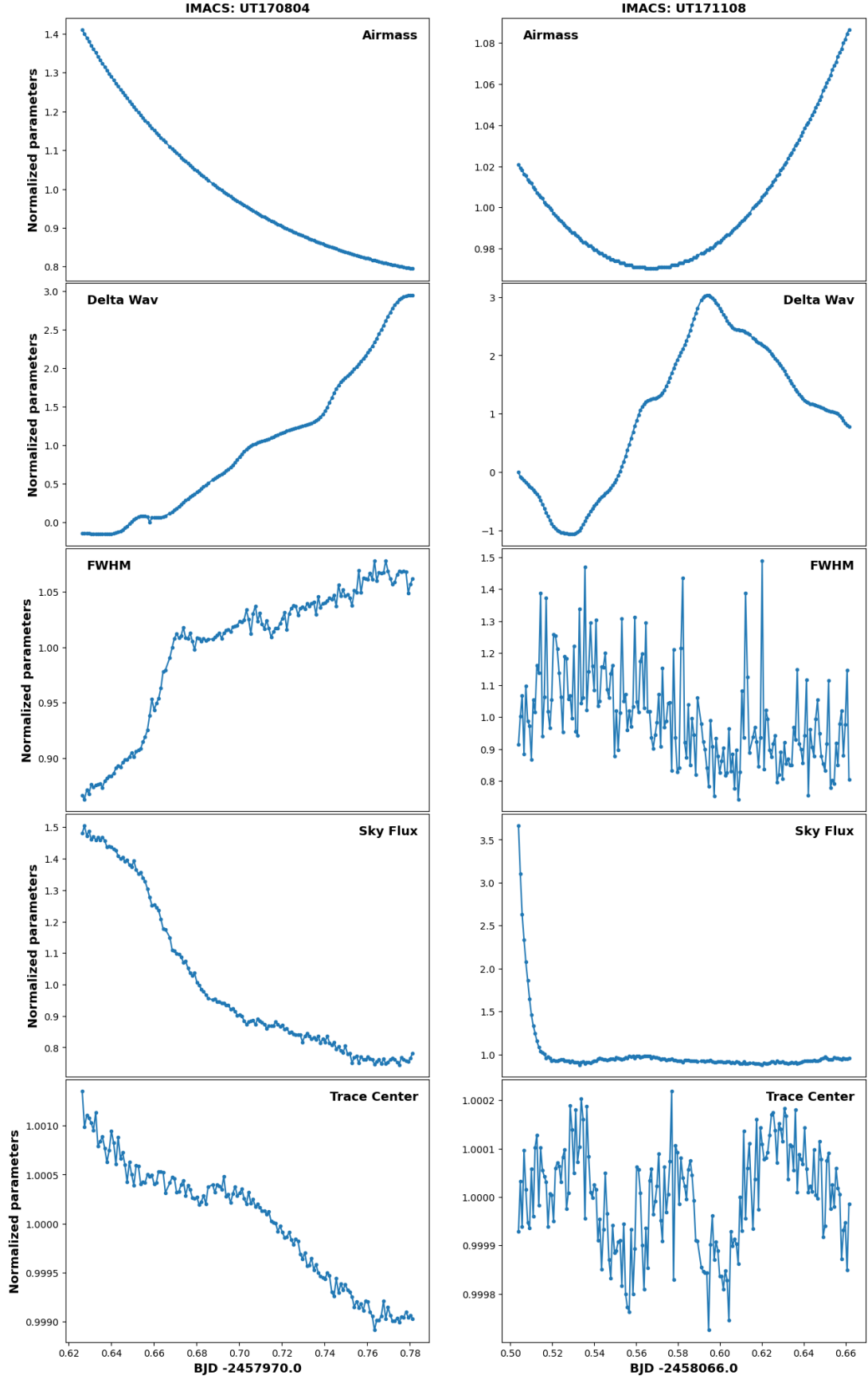


Figure 15. The mean normalized external parameters of the IMACS observations, used to correct for systematics in both the detrending methods (PCA+GP and CMC+Poly). The left column are the external parameters for UT170804 and the right is for UT171108. The rows correspond to the change in air mass, drift of the wavelength solution, FWHM of the target spectra, mean sky flux, and position of the central pixel trace (perpendicular to the dispersion axis), respectively. Plots of the FORS2 external parameters can be seen in [Nikolov et al. \(2018\)](#) Extended Data Fig. 4

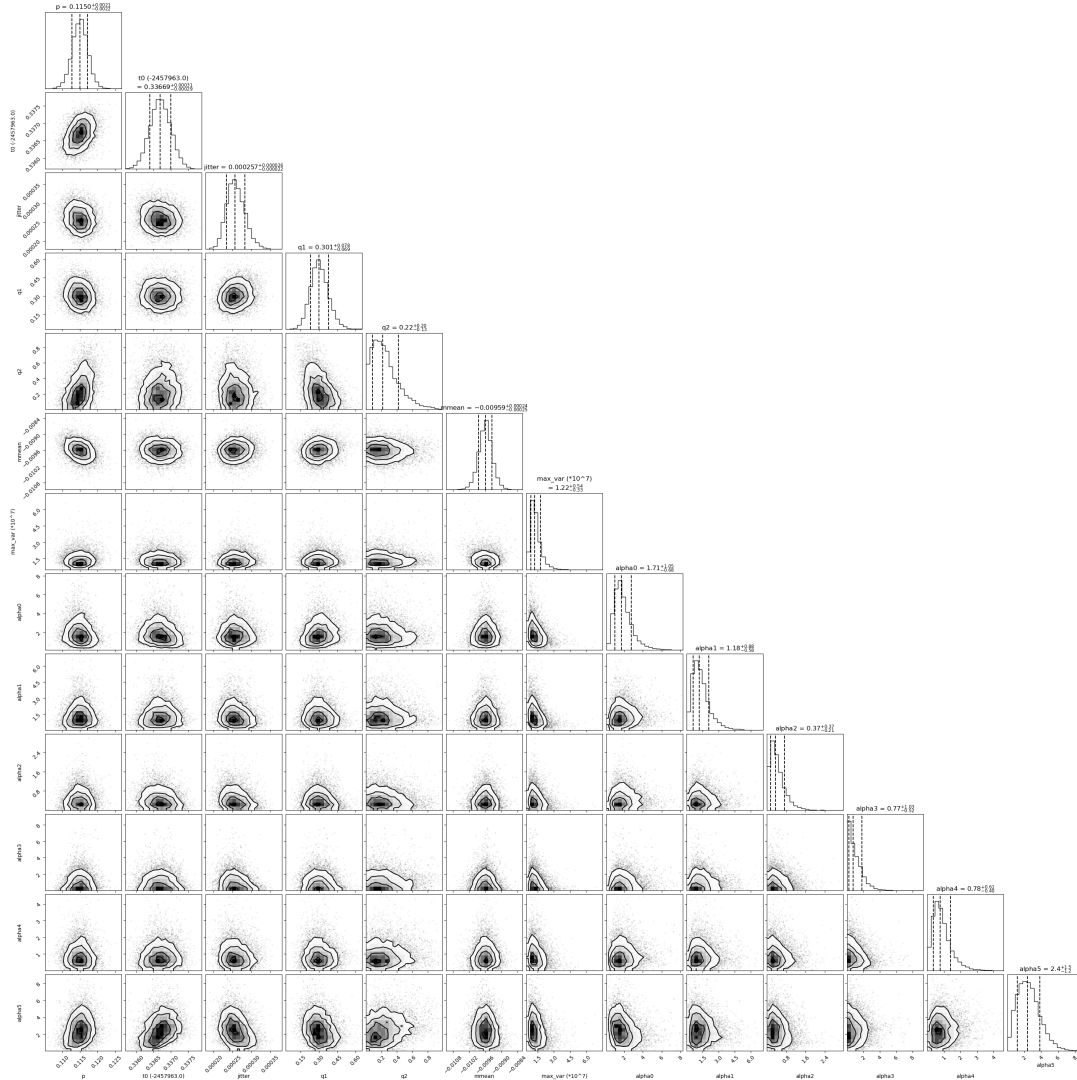


Figure 16. Corner plot of the GP fit on the FORS2 600B blue grism (UT170729) white-light light curve. The white light curve fit is used to create the final CMC term and this posterior corresponds to the fit shown in the first column of Figure 2. This would also be the same detrending routine used to detrend the binned data, if the GP (PCA+GP for the IMACS data) routine was used rather than the CMC routine. The alphas are the GP inverse squared length-scales on the external parameter regressors. Alphas 0 to 5 correspond to the target dispersion drift, cross-dispersion drift, variation of the FWHM, air mass, mean sky flux, rotator angle.

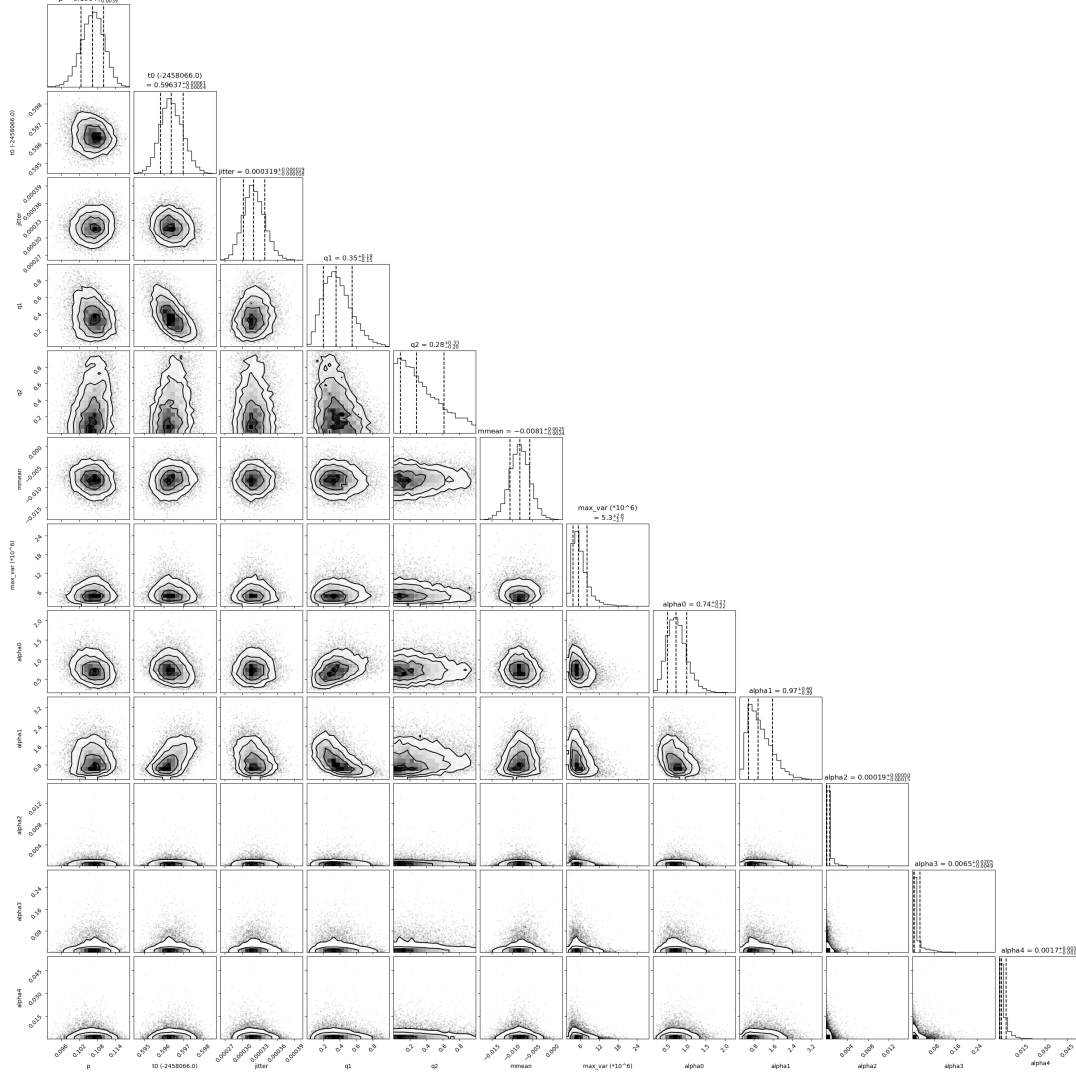


Figure 17. Same as Figure 16 but for the second IMACS transit (UT171108). Here Alphas 0 to 4 correspond to air mass, drift of the wavelength solution, FWHM, mean sky flux, and central trace.

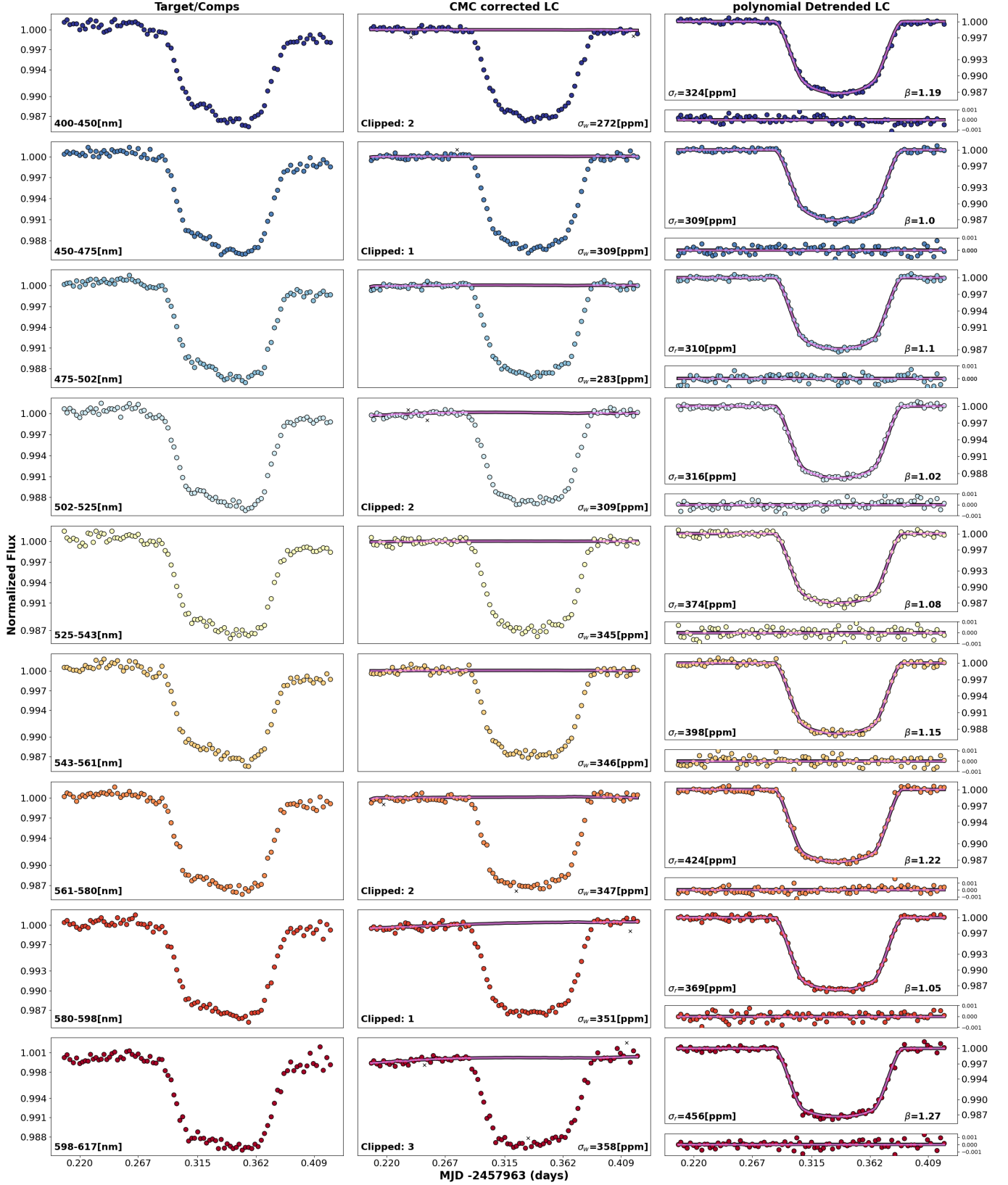


Figure 18. **Left:** Raw binned light curves (LC) of VLT/FORS2 transit UT170729 produced by dividing the comparison star LC (or the sum of the comparison star LC, in the case of the IMACS data) by the target's. The wavelength range of each bin is printed in the bottom left corner. **Middle:** LC produced by dividing the raw LC by the Common Mode Correction (CMC) term shown in Figure 2 (final row). The number of sigma clipped points is printed in the bottom left and those points are marked with a black x, the theoretical photon noise precision is also printed as σ_w . The additional polynomial systematic correction specifically fit for each bin is shown as a magenta line. **Right:** The final CMC and polynomial corrected light curve, with the best fit transit model in magenta and the residuals of the detrended data from the best-fit transit model on the bottom. The standard deviation (σ_r) of the residuals in ppm is printed in the bottom left corner and the ratio of σ_r and σ_w (β) is printed.

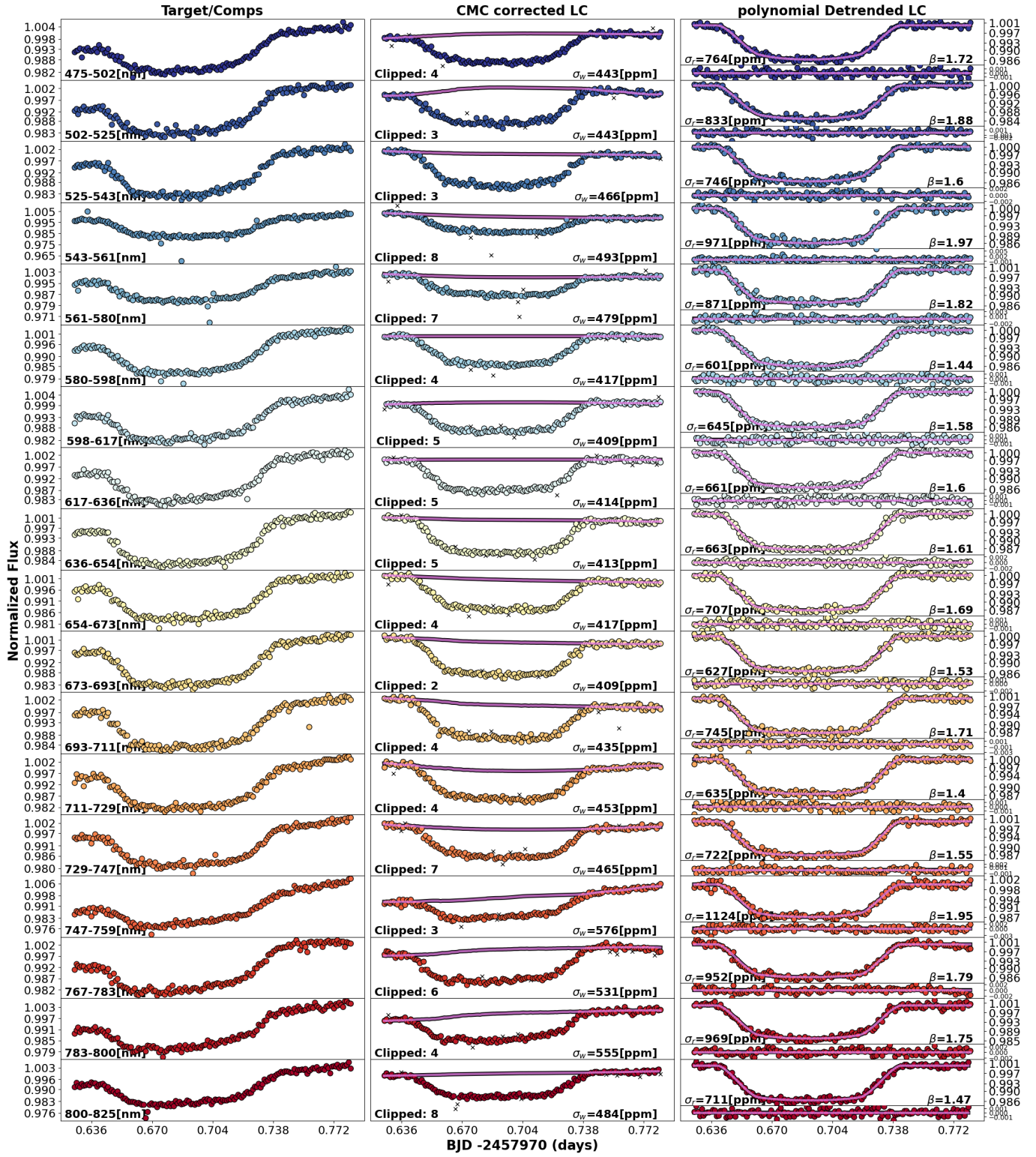


Figure 19. Same as Figure 18, but for Magellan/IMACS transit UT170804.

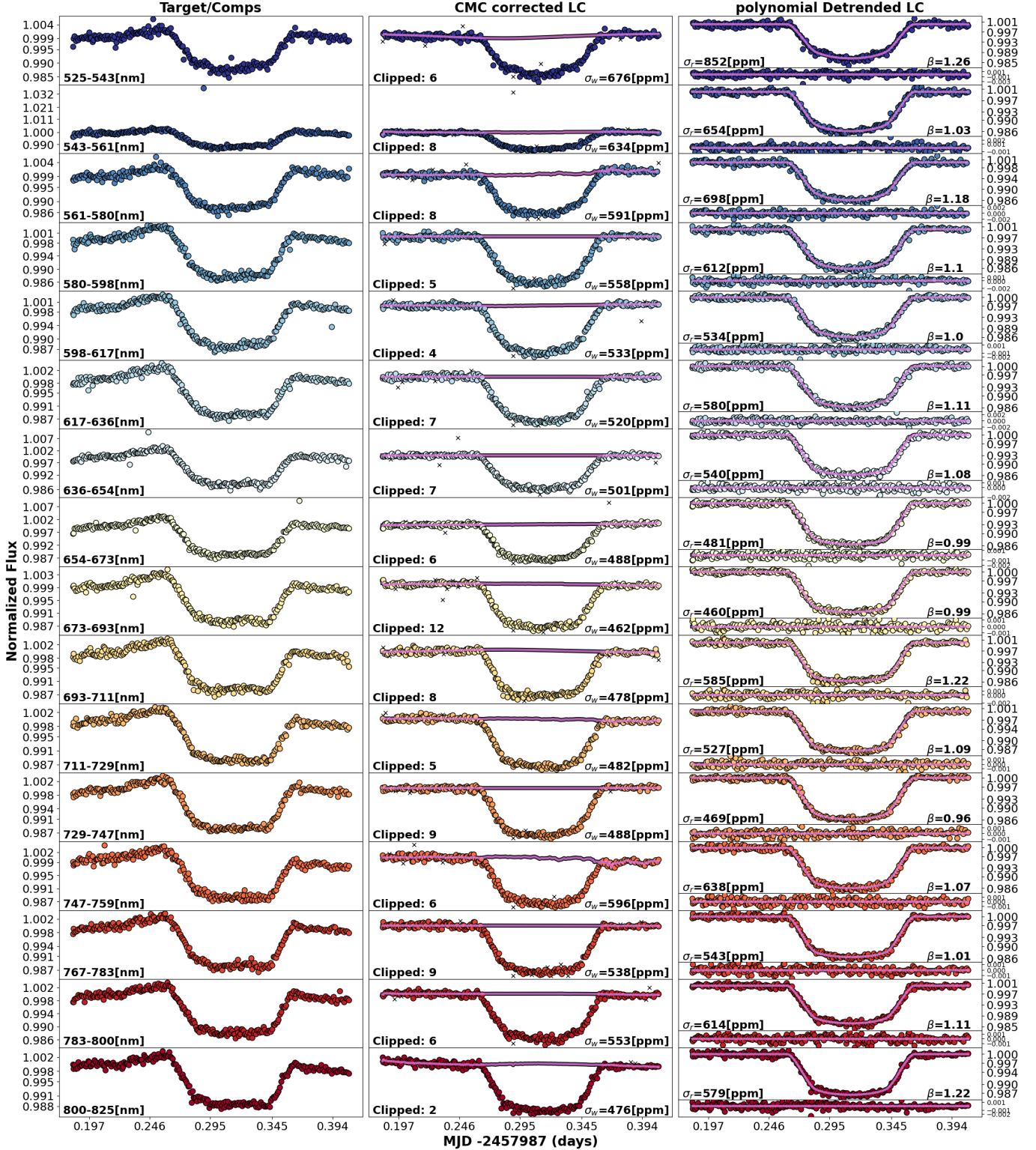


Figure 20. Same as Figure 19, but for VLT/FORS2 transit UT170822. Though there are a few cases (8th, 9th, and 12th bins) where β is slightly less than one. We do not interpret this as the light curve was over corrected, but given that they are nearly one, we see this as we achieved photon noise precision for those bins.

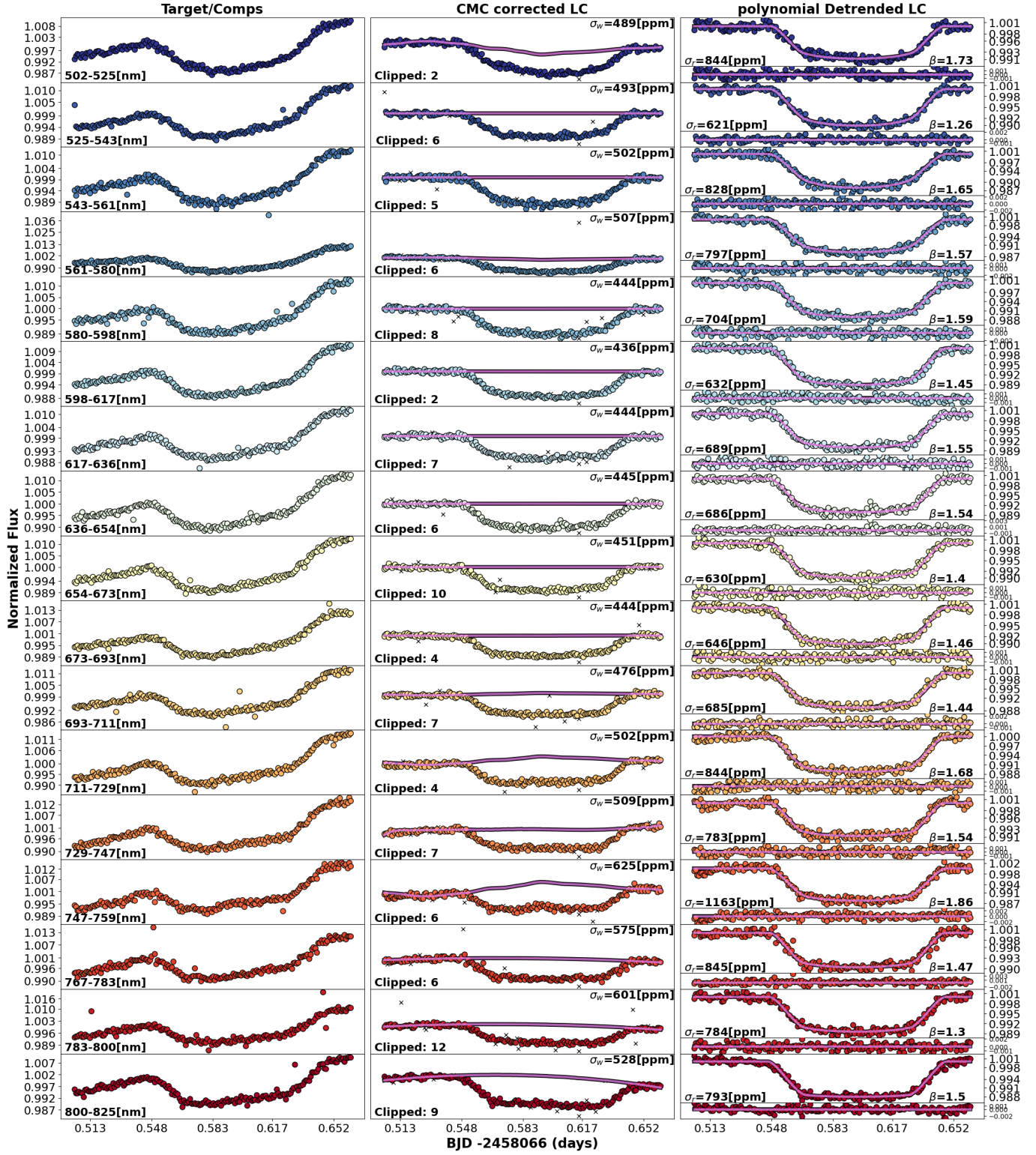


Figure 21. Same as Figure 20, but for Magellan/IMACS transit UT171108.

Table 9. Near-IR transmission spectrum obtained from Yip et al. (2021). The G102 grism is from 8000–11250 Å and the G141 grism is from 11372–12180 Å.

Wavelength (Å)	R_p/R_s	Wavelength (Å)	R_p/R_s
8000.00 – 8250.00	0.116327 ± 0.000772	12370.00 – 12559.00	0.117175 ± 0.000650
8250.00 – 8500.00	0.117499 ± 0.001021	12559.00 – 12751.00	0.117512 ± 0.000790
8500.00 – 8750.00	0.117439 ± 0.000940	12751.00 – 12944.00	0.119013 ± 0.000780
8750.00 – 9000.00	0.117597 ± 0.001338	12944.00 – 13132.00	0.117490 ± 0.000816
9000.00 – 9250.00	0.117473 ± 0.001331	13132.00 – 13320.00	0.118453 ± 0.000971
9250.00 – 9500.00	0.118305 ± 0.000801	13320.00 – 13509.00	0.118013 ± 0.000765
9500.00 – 9750.00	0.116508 ± 0.000883	13509.00 – 13701.00	0.118878 ± 0.000717
9750.00 – 10000.00	0.117490 ± 0.000919	13701.00 – 13900.00	0.120121 ± 0.000995
10000.00 – 10250.00	0.117427 ± 0.000850	13900.00 – 14100.00	0.120768 ± 0.001002
10250.00 – 10500.00	0.118545 ± 0.000915	14100.00 – 14303.00	0.119470 ± 0.000865
10500.00 – 10750.00	0.117456 ± 0.001000	14303.00 – 14509.00	0.119771 ± 0.000800
10750.00 – 11000.00	0.118174 ± 0.000594	14509.00 – 14721.00	0.117461 ± 0.000970
11000.00 – 11250.00	0.119214 ± 0.000466	14721.00 – 14941.00	0.118351 ± 0.000776
11153.00 – 11372.00	0.117894 ± 0.000689	14941.00 – 15165.00	0.118482 ± 0.000924
11372.00 – 11583.00	0.118786 ± 0.000845	15165.00 – 15395.00	0.117843 ± 0.000809
11583.00 – 11789.00	0.118811 ± 0.000887	15395.00 – 15636.00	0.116880 ± 0.000661
11789.00 – 11987.00	0.117792 ± 0.000771	15636.00 – 15889.00	0.118089 ± 0.000722
11987.00 – 12180.00	0.116893 ± 0.000932	15889.00 – 16153.00	0.117456 ± 0.001005
12180.00 – 12370.00	0.117520 ± 0.000897	16153.00 – 16436.00	0.117435 ± 0.000928

E. SYNTHETIC SPECTRA

In our initial analysis, we reduced the VLT/FORS2 transmission spectrum using the PCA+GP routine (just ‘GP’, given that there is only one comparison), discussed in appendix B.1, to reduce the white light curves and the binned light curves. When comparing the VLT/FORS2 transmission spectrum produced with this method to the original spectrum (Nikolov et al. 2018), shown in Figure 22. We found that the uncertainties from the GP method were over 3 times larger than when Nikolov et al. (2018) used their CMC+Poly method on the same data. This was independent of if the squared exponential kernel (see Appendix B.1) or the *george* Matern32Kernel was used. Naturally, this is concerning, because though both methods produce similar overall structures, Figure 22 implies that either CMC+Poly underestimates the uncertainties or GP overestimates it. As such, we test the accuracy and precision of both methods using synthetic data.

The first step to produce our synthetic data was to generate a transit light curve with parameters similar to what produces the transit light curve of WASP-96b. For generating all light curves we used *batman* (Kreidberg 2015) with the same time stamps as FORS2 transit UT170729 (i.e. 90 points covering ~ 5 hours). The exact light curve parameters used are shown in Table 10.

Next, we generated a realization of a Gaussian Process, GP(t , instrumental_systematics), for the common systematics that affect all spectrophotometric bands. Here the ‘instrumental_systematics’ were the FORS2 transit UT170729 auxiliary parameters of airmass, full-width at half-maximum (FWHM), and rotational angle. Using *george* (Foreman-Mackey et al. 2014), we combined three squared exponential kernels each with an inverse natural-log length scale of -2 and a constant term of -5, -12, and -12 for the GP inputs of airmass, FWHM, and rotational angle, respectively. The values of the inverse length scale and constant terms were empirically deduced in order to produce systematics with amplitudes and structure similar to what was seen in the FORS2 transit UT170729 light curves. An example of the white light curve and its GP systematics is shown in Figure 23.

Our third step, was to produce the binned light curves. This was done by generating 10 light curves each containing the same GP systematic realization as above, but with quadratic limb darkening (LD) coefficients determined using *PyLDTk* (Parviainen & Aigrain 2015) with a stellar effective temperature of 5500 K, stellar $\log_{10}(g)$ of 4.42, metallicity ($\log_{10}(Z)/\log_{10}(Z_{\odot})$) of 0.25 dex, and assuming each bin was 150Å wide starting from 3800 to 5300Å. Each binned light curve had a unique realization

of shot noise with a 400 ppm standard deviation. In addition, each binned light curve had a unique systematic added by generating a first order polynomial on dispersion drift, a second order polynomial on cross-dispersion drift, and a first order polynomial on rotator angle. The coefficients of each polynomial on each bin were randomly drawn from a uniform distribution from -0.1 to 0.1. Each polynomial function was standardized (a common practice done by e.g. Evans et al. 2017; Espinoza et al. 2019b; Kirk et al. 2021, etc.) and their product was used as the chromatic systematics. An example of binned light curves and their polynomial systematics can be seen in Figure 24.

The final step in producing the synthetic data was to decompose the light curves into two components, the target light curves and the comparison star light curves. When making the comparison star light curve we take a constant light curve with normalized value of 1 and add a separate draw from the above GP systematics, i.e. using the same auxiliary parameters and kernels, but a different random draw from the GP distribution. Because it is assumed that the systematics affecting the comparison star’s light curve should also affect the targets, we multiple this GP draw by the original target light curve. Thus, when the target is divided by the comparison, the effect of the comparison’s systematics are completely divided out. This might not happen in real datasets, because the comparison could add additional systematics, but for our synthetic data, we assume any such systematics is included in the initial construction of the light curve (i.e. the first GP draw). The first column of Figure 24 shows examples of synthesized binned target light curves and comparison light curves. The white light curve can then be constructed by combining all 10 bins, and assuming each bin had the same number of counts. When producing all synthetic data we followed these steps 50 times, where each white light curve was produced with a different draw from the GP distribution, unique realizations of shot noise, and unique coefficients for the polynomial systematics on each bin.

F. RETRIEVAL MODELING PRIORS

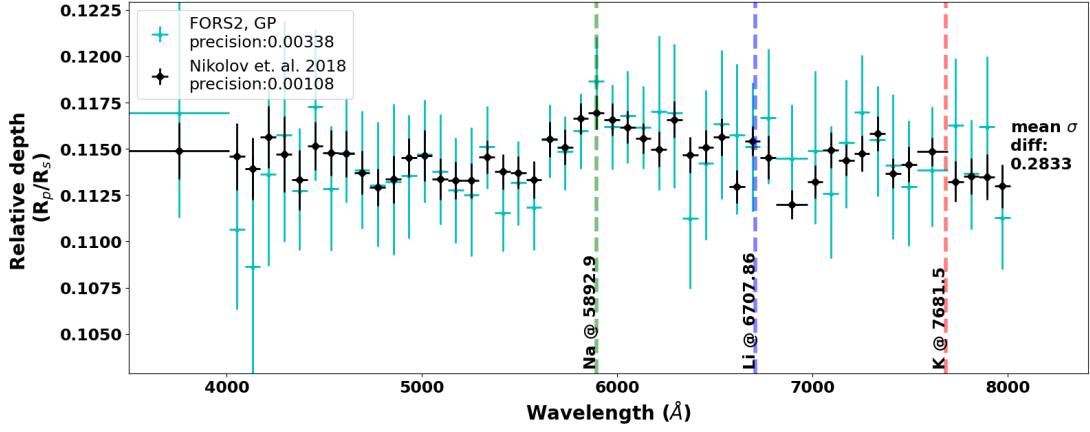


Figure 22. The transmission spectra of VLT/FORS2 data. The black diamonds with uncertainties is the analysis done by Nikolov et al. (2018), and the cyan dots with uncertainties is our initial analysis of the VLT/FORS2 data with the same wavelength bins and using the GP detrending method. An offset is applied so their mean depths are equal to one another. Each spectrum is a weighted average of observations taken with the B filter (350–617.3 nm) on the night of UT170729 and the R filter (529.3–801.3 nm) on the night of UT170822. The average deviation of each point relative to their uncertainties is 0.28σ , suggesting that the spectral structures are the same.

Table 10. The initial transit parameters to construct the synthetic data (column 2), the white-light priors used when fitting the data (column 3), and the binned priors (column 4). The period (P) of 3.42526 days and mid transit time (t_0) of 2457963.336499 days were held fixed for all fits. Here 'b' is the impact parameter, which can be transformed to inclination (i) via equation 1 using a/R_s , eccentricity (fixed at 0), and ω (fixed at 90°). The limb-darkening parameters were determined using PyLDTk and were different for each bin, what is shown in the table below is the average.

parameter	value	white-light	binned
R_p/R_s	0.1157	uniform: 0.1–0.14	normal: m=(WL fit), $\sigma_n = 0.05$
$\langle q_1 \rangle$	0.8208	uniform: 0–1	uniform: 0–1
$\langle q_2 \rangle$	-0.0201	uniform: 0–1	uniform: 0–1
b	0.7456	uniform: 0.5–1	Fix to WL fit
a/R_s	9.0	uniform: 8–10	Fix to WL fit

Table 11. The priors for **Exoretrievals** and **PLATON**. These priors were set to allow for a wide parameter space to be surveyed, but contained within physical regimes. Not all parameters were included in each model fit (see Tab. 7). We used 5000 live points for all runs. For further description of the parameters of **Exoretrievals**, please refer to the Appendix D of [Espinoza et al. \(2019b\)](#). The log cloud absorbing (σ_{cloud}) parameter was fixed because across all datasets and all models which included aerosols, this retrieved parameter was near -55. As such, we decided to reduce the dimensionality of the explored posterior space by fixing it to this value, effectively turning off clouds.

Exoretrievals			PLATON		
parameter	function	bounds	parameter	function	bounds
reference pressure (P_0 , bars)	log-uniform	-8 to 3	reference pressure (P_{clouds} , Pa)	log-uniform	-3.99 to 7.99
planetary atmospheric temperature (T_p)	uniform	500 to 1600K	planetary atmospheric temperature (T_p)	uniform	500 to 1600K
stellar temperature (T_{occ})	uniform	5300 to 5780K	stellar temperature (T_{star})	gaussian	$\mu=5540K, \sigma=150K$
stellar heterogeneities temperature (T_{het})	uniform	2540 to 8540K	stellar heterogeneities temperature (T_{spot})	uniform	2540 to 8540K
heterogeneity covering fraction (f_{het})	gaussian	$\mu=0.014, \sigma=0.009$	heterogeneity covering fraction (f_{spot})	gaussian	$\mu=0.014, \sigma=0.009$
offset (depth)	gaussian	$\mu=0, \sigma=2000ppm$	offset (depth)	uniform	-6000 to 6000ppm
haze amplitude (a)	log-uniform	-1 to 10	scattering factor	log-uniform	-10 to 10
haze power law (γ)*	uniform	-14 to 4	scattering slope (α) [†]	uniform	-4 to 14
log cloud absorbing cross-section (σ_{cloud})	Fixed	-55	metallicity (Z/Z_\odot)	log-uniform	-1 to 3
trace molecules' mixing ratios	log-uniform	-30 to 0	C/O	uniform	0.05 to 2
reference radius factor(f) [◇]	uniform	0.8 to 1.2	1 bar, reference radius (R_0)	uniform	1 to 1.4 R_j

*This is the exponent of the scattering slope power law, where -4 is a Rayleigh scattering slope.

[†]This is the wavelength dependence of scattering, with 4 being Rayleigh.

[◇]This is a factor multiplied by the inputted planetary radius to produce the reference radius, i.e. $R_0 = fR_p$

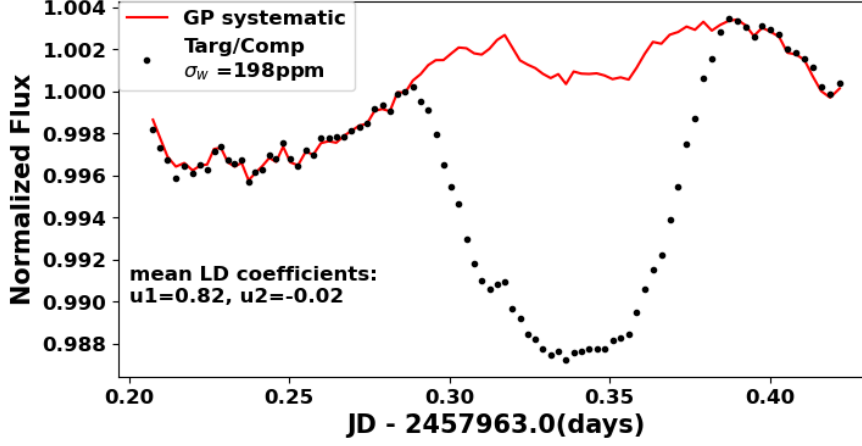


Figure 23. An example synthetic white light curve (black dots) constructed by adding all 10 binned light curves in Figure 24. Given that all of the individual chromatic systematics are smaller relative to the white-light systematics and the transit, we do not see their effect in this light curve. This is exactly what we would see in a true light curve (e.g. see Fig. 2). The red line is the systematics produced by a random draw from a GP distribution created using airmass, full-width at half-maximum (FWHM), and rotational angle as inputs. σ_w is the residuals of the out-of-transit data from the GP systematic model, which would be 0 if there was no white noise added.

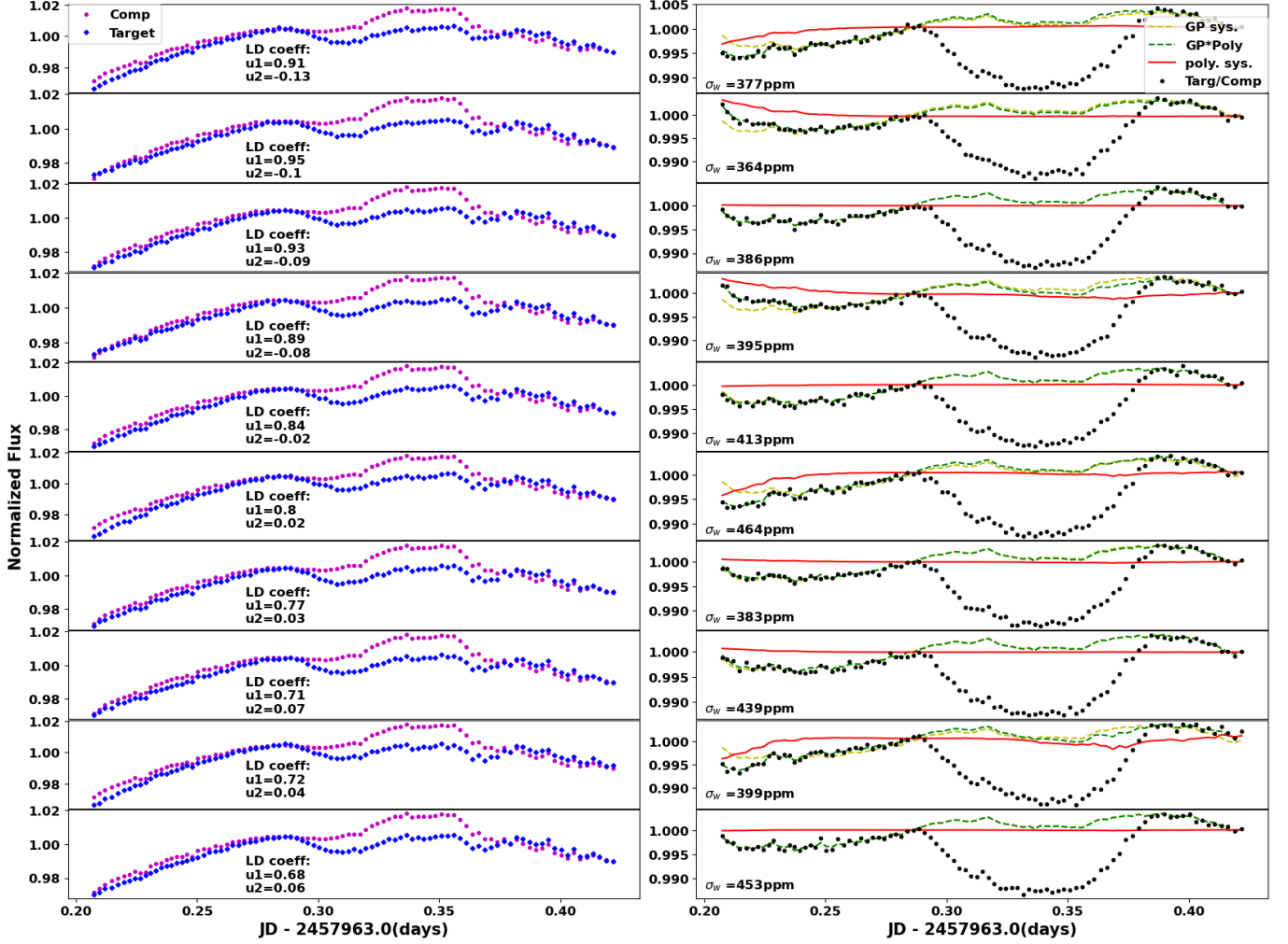


Figure 24. The specific binned light curve used to construct the WLC in Figure 23. The left column shows the binned target light curves (blue) and the binned comparison light curves (purple). The target light curve is composed of the transit, systematics common to all bins and the comparisons, systematics common to all bins and just the target, and systematics unique to each bin. The LD coefficients used for each bin are printed below the light curves, and were determined with PyLDTk. The right column shows the 'raw' (target/comparison) light curve in black dots. The larger amplitude GP systematics (constant for each bin) is shown as a yellow dashed line, the smaller amplitude polynomial systematics (unique per bin) is shown in red and the combined GP and polynomial systematics is shown as green dashes. The residuals of the out-of-transit data from the green dashed line is printed in the bottom left corner (σ_w).